Actomyosin activity-dependent apical targeting of Rab11 vesicles reinforces apical constriction

Wei Chen and Bing He*

Department of Biological Sciences, Dartmouth College, Hanover, NH, 03755, USA

* Correspondence to: bing.he@dartmouth.edu

Running title:

Feedback via Rab11 reinforces apical constriction

10 ***Abstract:***

11 During tissue morphogenesis, cell shape changes resulting from cell-generated forces often
12 require active regulation of intracellular trafficking. How mechanical stimuli influence
13 intracellular trafficking and how such regulation impacts tissue mechanics are not fully
14 understood. In this study, we identify an actomyosin dependent mechanism involving Rab11-
15 mediated trafficking in regulating apical constriction in the *Drosophila* embryo. During
16 *Drosophila* mesoderm invagination, apical actin and Myosin II (actomyosin) contractility
17 induces apical accumulation of Rab11-marked vesicle-like structures ("Rab11 vesicles") by
18 promoting a directional bias in dynein mediated vesicle transport. At the apical domain,
19 Rab11 vesicles are enriched near the adherens junctions (AJs). The apical accumulation of
20 Rab11 vesicles is essential to prevent fragmented apical AJs, breaks in the supracellular
21 actomyosin network and a reduction in the apical constriction rate. This Rab11 function is
22 separate from its role in promoting apical Myosin II accumulation. These findings suggest a
23 feedback mechanism between actomyosin activity and Rab11-mediated intracellular
24 trafficking that regulates the force generation machinery during tissue folding.

Introduction:

Cell-generated mechanical forces play a central role in tissue morphogenesis. Genetically prescribed cellular forces can drive cell shape change and cell motion as a direct physical outcome, thereby mediating spatially and temporally defined tissue deformation (Collinet and Lecuit, 2021; Gilmour et al., 2017). In addition, mechanical forces can impact morphogenesis by triggering various cellular activities ranging from cytoskeleton reorganization to changes in gene expression (Fletcher and Mullins, 2010; Kirby and Lammerding, 2016; Sun and Irvine, 2016; Uhler and Shivashankar, 2017). Such active processes allow cells and tissues to respond to mechanical inputs adaptively and thereby increase the robustness of tissue morphogenesis. However, our knowledge of the active response of cells to mechanical forces remains limited.

In this work, we used mesoderm invagination during *Drosophila* gastrulation as a model to study how cells respond to contractile forces generated by actomyosin networks. Immediately before gastrulation, *Drosophila* embryos undergo an atypical cleavage called cellularization, during which peripherally localized syncytial nuclei are partitioned into a monolayer of epithelial cells (Mazumdar and Mazumdar, 2002). Mesoderm invagination is initiated by apical constriction resulted from graded apical activation of actomyosin in a 12-cell wide region in the ventrally localized mesodermal primordium (Heer et al., 2017; Leptin and Grunewald, 1990; Lim et al., 2017; Sweeton et al., 1991). These cells subsequently invaginate as the epithelium bends inwards, resulting in the formation of a furrow on the

46 ventral side of the embryo. The upstream signaling pathway that activates apical constriction
47 has been well characterized (reviewed in Gheisari et al., 2020; Gilmour et al., 2017; Martin,
48 2020). In response to the dorsal-ventral patterning information, the prospective mesodermal
49 cells express two transcription factors, Twist and Snail, which in turn trigger the apical
50 recruitment and activation of RhoGEF2 through GPCR signaling (Jha et al., 2018; Kerridge
51 et al., 2016; Manning et al., 2013). RhoGEF2 further activates the small GTPase Rho1 (the
52 *Drosophila* homologue of RhoA) and leads to the activation of Myosin II through Rho1's
53 effector Rho-associated protein kinase (Rok). Activated Myosin II forms an supracellular
54 actomyosin network at the apical cortex that is interconnected across the tissue through apical
55 adherens junctions (AJs) (Amano et al., 1996; Dawes-Hoang et al., 2005; Kimura et al.,
56 1996; Mason et al., 2013; Nikolaidou and Barrett, 2004; Vasquez et al., 2014; Winter et al.,
57 2001). Within individual cells, the contractions of apical actomyosin network pull AJ sites
58 inwards, causing progressive apical cell area reduction (Martin and Goldstein, 2014; Martin
59 et al., 2009; Martin et al., 2010; Mason et al., 2013).
60
61 Apical constriction can drive reorganization from subcellular to tissue levels through both
62 active and passive means. Apical constriction drives a tissue-scale viscous flow at the tissue
63 interior (He et al., 2014). Certain organelles, such as the nucleus, appear to move passively
64 with the flow by advection (Gelbart et al., 2012). Other subcellular structures, in contrast,
65 undergo active reorganization in response to apical forces. For examples, apical actomyosin
66 contractility has been shown to mediate apical shift and stabilization of the AJs and promote

67 the formation of a medioapically-localized noncentrosomal microtubule-organization center
68 (Weng and Wieschaus, 2016; Ko et al., 2019). It remains unclear whether other subcellular
69 structures also undergo active remodeling in response to apical constriction.
70
71 Rab11, a small GTPase of the Rab family, is a well-established marker for recycling
72 endosomes (Welz et al., 2014). Like typical small GTPases, Rab11 switches between active
73 and inactive states depending on the phosphorylation state of its bound guanine nucleotide. In
74 addition to recycling endosomes, Rab11 has also been reported to localize to the trans-Golgi
75 network (TGN) and post-Golgi vesicles. It functions in both exocytic and endocytic recycling
76 pathways by regulating vesicular transport from TGN and recycling endosomes to the plasma
77 membrane (Benli et al., 1996; Chen et al., 1998; Jedd et al., 1997; Pelissier et al., 2003;
78 Takahashi et al., 2012; Ullrich et al., 1996; Welz et al., 2014). Rab11 regulates multiple
79 vesicular trafficking steps, including vesicle formation, transport and tethering through its
80 various downstream effectors. For example, Rab11 directly interacts with the actin motor
81 Myosin V (Lapierre et al., 2001; Lipatova et al., 2008). It can also form complexes with
82 microtubule motors dynein and kinesins through adaptor proteins (Welz et al., 2014). These
83 interactions allow Rab11 vesicles to be transported along both actin and microtubule
84 filaments (Horgan et al., 2010; Schonteich et al., 2008; Schuh, 2011; Wang et al., 2008).
85
86 Here, we present evidence that apical actomyosin contractility induces biased transport of
87 Rab11-positive vesicles towards the cell apex in a dynein- and microtubule-dependent

88 manner. At the apical side, Rab11 vesicles are enriched at the vicinity of AJs. Eliminating
89 these vesicles through acute inactivation of Rab11 results in defects in AJ organization and
90 breaks in the supracellular actomyosin network. Our findings reveal an intimate interplay
91 between apical actomyosin contractions and Rab11-mediated vesicle trafficking that serves as
92 a feedback mechanism to reinforce the structural integrity of the apical actomyosin network.
93

Results:

Rab11 accumulates apically in the constricting cells during ventral furrow formation

In a search for potential changes in subcellular organization induced by apical actomyosin contractions, we found that Rab11-labeled compartments undergo prominent reorganization during apical constriction (Figure 1A-E; Figure S1). Live imaging of embryos expressing endogenously YFP-tagged Rab11 and image segmentation (Berg et al., 2019; Methods) revealed two main types of Rab11-positive structures (Figure 1F, G; Figure S1B): (1) One or a few large perinuclear compartments residing at the apical side of each nucleus (hereafter "perinuclear Rab11 compartment"). These compartments likely represented the trafficking intermediate described in a previous study based on similarities in morphology and localization (Pelissier et al., 2003). And (2) Small punctate structures. These puncta were less than 1 μm in diameter and appeared as diffraction limited spots. Based on previous literature, these Rab11 puncta could be small transport vesicles, recycling endosomes and/or other type of transport carrier (Welz et al., 2014) ("Rab11 vesicles" herein). Before gastrulation, Rab11 vesicles were present near the basal side of the perinuclear Rab11 compartments (Figure 1C, 0 min; Figure 1F, G, 0 min). As the cells constricted apically, perinuclear Rab11 compartments moved basally following the basal movement of the nuclei (Figure 1C, blue outlines, 9 min; Figure 1F, G, 7 min). Meanwhile, Rab11 vesicles appeared near the cell apices and accumulated apically (Figure 1C-G). The difference in Rab11 vesicle distribution before and after apical constriction was further confirmed by quantification of Rab11 vesicle intensities at various apicobasal positions (Figure 1H; Methods). The Rab11 vesicles were

115 highly dynamic, yet at any given time the majority accumulated either adjacent to or slightly
116 basal to the apical actomyosin network (Figure 1E). No apical accumulation of Rab11
117 vesicles was observed in the surrounding ectodermal cells that did not undergo apical
118 constriction (Figure 1C; Figure S1A). In addition, we did not observe obvious apical
119 enrichment in the constricting cells for the other organelles we examined (Figure S1C-H).
120 The apical enrichment of Rab11 vesicles could not be readily explained by cytoplasmic
121 advection and suggests the involvement of active regulation.
122

123 **Apical accumulation of Rab11 vesicles depends on apical actomyosin network but does**
124 **not require intact adherens junctions or apical shrinking**

125 The spatiotemporal correlation between the apical Myosin II activation and the apical
126 accumulation of Rab11 vesicles prompted us to examine the relationship between the two
127 processes. To test whether apical activation of Myosin II is required for apical accumulation
128 of Rab11 vesicles, we injected embryos with the Rok inhibitor Y-27632 (Narumiya et al.,
129 2000). Injection of Y-27632 at the end of cellularization completely prevented apical Myosin
130 II activation and abolished apical Rab11 vesicle accumulation (Figure 2A). Next, we adapted
131 a previously described on-stage injection protocol (Coravos and Martin, 2016) to test the
132 effect of Y-27632 injection on Rab11 vesicles after they accumulated apically. After drug
133 injection, Myosin II immediately (< 1 min) dissociated from the apical cortex (Figure 2B,
134 B'). About 4 minutes after injection, Rab11 vesicles were largely depleted from the apical
135 surface (Figure 2B). The morphology of perinuclear Rab11 compartments was not obviously

136 affected by Y-27632 injection (Figure 2B, 3 – 6 μm). Consistent with the Y-27632 treatment,
137 knockdown of the myosin heavy chain Zipper also inhibited apical Rab11 vesicle
138 accumulation (Figure 2C). Together, these observations indicate that the induction and
139 maintenance of apical accumulation of Rab11 vesicles depends on the recruitment and/or
140 activation of apical Myosin II. In further support of this notion, we found that an expansion
141 of the actomyosin activation domain in ventralized *Spn27A* mutant embryos resulted in a
142 similar expansion of the region with apical accumulation of Rab11 vesicles (Figure 2D;
143 Ligoxygakis et al., 2003).
144
145 Since cortical actin network is required for Myosin II to generate contractile forces (Martin et
146 al., 2009), we asked whether apical Rab11 vesicle accumulation depends on F-actin. To this
147 end, we injected embryos with cytochalasin D (cytoD) to acutely disrupt actin network
148 during apical constriction. Upon cytoD injection, the apical side of the constricted cell
149 immediately relaxed, suggesting a rapid loss of myosin contractility (Figure 3A; Video 1).
150 Interestingly, Myosin II remained enriched apically in the first four minutes after injection
151 (Figure 3A). In contrast, apical Rab11 vesicles quickly diminished after injection, similar to
152 what we observed in Y-27632 injected embryos (Figure 3B). This result indicates that the
153 accumulation of Myosin II at the apical domain is not sufficient to induce apical Rab11
154 vesicle accumulation without F-actin. Together, our observations so far suggest that an intact,
155 contractile apical actomyosin network is critical for apical accumulation of Rab11 vesicles.
156

157 During ventral furrow formation, contractile forces generated by apical actomyosin network
158 result in progressive apical shrinking in the presumptive mesoderm and a buildup of apical
159 tension across the constriction domain, both require apical AJs (Martin et al., 2009; Martin et
160 al., 2010; Mason et al., 2013). We therefore asked whether apical shrinking or the presence of
161 intact AJs is required for apical accumulation of Rab11 vesicles. We found that knockdown of
162 α-Catenin, a core component of AJ complex, did not prevent Rab11 vesicle accumulation,
163 although this treatment impaired the connection between the actomyosin network and the cell
164 membrane, causing Myosin II to coalesce into clustered spots at the center of the medioapical
165 domain (Martin et al., 2010; Figure 3C). In addition, we found that induction of apical
166 actomyosin contractility in dorsal cells without accompanying apical shrinking through Fog
167 overexpression (Morize et al., 1998; Methods) is sufficient to induce apical accumulation of
168 Rab11 vesicles (Figure 4A-C). Finally, we found that apical shrinking during dorsal fold
169 formation, a Myosin II-independent tissue folding process (Wang et al., 2012), did not induce
170 apical accumulation of Rab11 vesicles (Figure 4D, E). Taken together, these results indicate
171 that the apical accumulation of Rab11 vesicles, which we have shown requires apical
172 contractile actomyosin network, does not depend on mesodermal cell fate, apical shrinking or
173 integration of tensile forces across the tissue.
174
175 **Rab11 vesicles undergo biased transport towards the cell apex during apical**
176 **constriction**
177 We next examined how Rab11 vesicles accumulate at the apical surface during apical

178 constriction. Apical endocytosis has been shown to play an important role in apical
179 constriction as the apical membrane shrinks over time (Lee and Harland, 2010; Mateus et al.,
180 2011; Miao et al., 2019). Rab11 vesicles may be derived from endocytosis of apical
181 membranes. However, when we chased endocytosed cell membrane using FM4-64, a
182 lipophilic dye (Methods), we barely detected any colocalization between FM4-64 positive
183 vesicles and Rab11 vesicles, although a majority of FM4-64 positive vesicles colocalized
184 with Rab5-marked early endosomes (Figure S2A-C, Video 2). Consistent with this
185 observation, we found that blocking endocytosis using the temperature sensitive mutant of
186 *shibire* (*shi*^{ts}), the *Drosophila* homolog of dynamin (van der Bliek and Meyerowrtz, 1991),
187 did not prevent apical accumulation of Rab11 vesicles (Figure S2D, E). Together, these
188 results indicate that endocytosed apical membrane is not the major source of apical Rab11
189 vesicles.
190
191 An intriguing possibility is that the apical Rab11 vesicles are supplied from the more basal
192 side of the cell by directional transport. To capture the rapid movement of Rab11 vesicles in
193 the apical-basal direction, we focused on the cells located near the medial-lateral boundaries
194 of the constricting domain. These cells are tilted towards the ventral midline at the late stage
195 of apical constriction, making it possible to follow the apical-basal movement of Rab11
196 vesicles by fast imaging of a single focal plane (Figure 5A). We always selected focal planes
197 where myosin could be observed at the medial side of the cells to ensure that the cells we
198 analyzed were accumulating myosin apically (Figure 5B). Using this approach, we observed

199 constant transport of Rab11 vesicles in the axial direction of the cells (Figure 5B). There were
200 both apically and basally directed movements, with a bias towards the apical direction.
201 Vesicle tracking revealed that the apically directed movement accounted for approximately
202 three quarters of the total transport events (74.5% ± 5.7%; n = 255 trajectories from 3
203 embryos, Figure 5C, D, G). Other than the bias in directionality, there was no significant
204 difference in other aspects of the trajectories between apical and basal transport, including the
205 average velocity, the duration and the travel distance of the tractable trajectories (Figure 5E).
206 To further validate the results, we imaged embryos expressing a membrane marker and
207 mCherry-Rab11 (overexpression), which allowed us to quantify transport events only in cells
208 undergoing apical constriction (Figure 5F, Methods). There was no significant difference
209 between the results from the two analyses (Figure 5G). Note that due to our imaging
210 configuration, our analysis of vesicle transport was limited to the apical portion of the cells
211 (typically above the nuclei) that bent over towards the midline. It is unclear whether Rab11
212 vesicle transport also exists at the more basal region of the cell. Taken together, our results
213 demonstrate that Rab11 vesicles undergo biased transport to the cell apex in cells with active
214 apical actomyosin contractions. This biased transport may account for the apical enrichment
215 of Rab11 vesicles in these cells.
216
217 **The apical-basal transport of Rab11 vesicles depends on microtubules and dynein**
218 Because the saltatory and directional movement of Rab11 vesicles was reminiscent of
219 microtubule-dependent transport, we asked whether the transport of Rab11 vesicles is

220 mediated by microtubules. By two-color imaging with mCherry-Rab11 and the microtubule
221 marker Jupiter-GFP (Karpova et al., 2006), we found that most Rab11 vesicles were
222 associated with microtubules or microtubule bundles as they moved apically or basally
223 (Figure 6A; Video 3). Furthermore, on-stage injection of colchicine, a microtubule
224 depolymerization drug, in gastrulating embryos resulted in a rapid (less than a minute) loss of
225 microtubules and a sharp reduction in the directional transport events. The remaining
226 transport events only occurred in regions with residual microtubules (Figure 6B; Video 3).
227 Together, these results demonstrate that the apical-basal transport of Rab11 vesicles is
228 microtubule dependent.
229
230 Next, we examined the impact of colchicine injection on the apical accumulation of Rab11
231 vesicles. In line with the observed role of microtubules in Rab11 vesicle transport, injection
232 of embryos at late cellularization (N = 5 embryos) resulted in a significant reduction in the
233 apical accumulation of Rab11 vesicles compared to control embryos (N = 4 embryos) (Figure
234 6C-F). The activation of apical Myosin II was normal in the injected embryos, consistent
235 with a recent report (Ko et al., 2019). Unexpectedly, injection of colchicine at or after the
236 onset of gastrulation (N = 5 embryos) resulted in a wider range of phenotypes, and on
237 average there was no significant reduction in the number of apically enriched Rab11 vesicles
238 (Figure 6C-F). We speculate that disruption of microtubules not only reduces the apical-basal
239 transport of Rab11 vesicles but also inhibits the turnover of the vesicles that are already
240 accumulated apically. This combined effect may obscure the effect of loss of microtubules

241 after the onset of gastrulation.

242

243 Finally, we tested the role of microtubule motor dynein on the transport of Rab11 vesicles.
244 We found that injection of antibody against the dynein intermediate chain (DIC) (Yi et al.,
245 2011) during apical constriction resulted in a rapid reduction of vesicle transport events in
246 both apical and basal directions, whereas injection of a control GST antibody had no effect
247 (Figure 6G, Video 4). Furthermore, the apical accumulation of Rab11 vesicles was greatly
248 reduced in dynein antibody-injected embryos but not in the control antibody-injected
249 embryos (Figure 6H). We were not able to perform similar test on the role of kinesin motors
250 due to a lack of functional reagents. However, the pronounced impact of dynein inhibition on
251 the transport and apical accumulation of Rab11 vesicles suggests that dynein plays a
252 predominant role in the apical-basal transport of Rab11 vesicles during apical constriction.
253 The observation that inhibiting dynein abolishes both apical and basal transport of Rab11
254 vesicles may reflect the bidirectional nature of the microtubule populations in the space
255 between cell apices and nuclei during apical constriction (Ko et al., 2019).

256

257 **The apical bias of Rab11 vesicle transport is rapidly abolished upon acute inhibition of**
258 **apical actomyosin contractility**

259 Because the apical enrichment of Rab11 vesicles depends on actomyosin activity, we asked
260 whether the biased basal-to-apical transport of Rab11 vesicles also depends on actomyosin
261 activity. To address this question, we used a recently developed optogenetic tool to acutely

262 inhibit actomyosin activity through blue light-induced recruitment of a dominant negative
263 form of Rho1 (Rho1DN) to the plasma membrane ("Opto-Rho1DN", Figure 7A; Guo et al.,
264 2021). Using the same imaging configuration as shown in Figure 5A, we examined the
265 immediate impact of actomyosin inhibition on the transport of Rab11 vesicles. As expected,
266 blue light stimulation resulted in rapid loss of apical Myosin II (within ~30 seconds; Figure
267 7B). The loss of apical Myosin II at this stage of ventral furrow formation did not cause
268 furrow relaxation or immediate changes in cell orientation. Strikingly, blue light stimulation
269 resulted in a rapid change in the transport of Rab11 vesicles. Within the first 23 seconds after
270 stimulation, the proportion of apical transport was 64.6% (64.6% ± 4.1%; n = 575 trajectories
271 from 3 embryos), lower than that in the wildtype controls (Figure 7C). This proportion
272 dropped to close to 50% (52.3% ± 2.0%; n = 645 trajectories from 3 embryos) in the next 23-
273 second time window, indicating that the directional bias was completely abolished (Figure
274 7C). Notably, the loss of directional bias was caused by an increase in the basal transport
275 events instead of a decrease in the apical transport events (Figure 7D, E). Other aspects of the
276 transport are comparable between the two time windows after stimulation (Figure 7F).
277 Therefore, the main effect of actomyosin inhibition on Rab11 vesicle transport is to increase
278 the basal transport events, which results in loss of apical bias of the transport.
279
280 The observation that the loss of transport bias upon actomyosin inactivation is caused by an
281 increase in the basal transport rather than a reduction in the apical transport suggests that the
282 effect is not due to a general disruption of the microtubule organization. In line with this

283 prediction, we did not observe obvious changes in the density or orientation of microtubules
284 within the first two-minute window after Opto-Rho1DN stimulation (Figure 7G, H). This
285 result is consistent with the previous report that medioapical MTOC only became obviously
286 affected a few minutes after cytoD injection (Ko et al., 2019). Together, these results suggest
287 that apical actomyosin network could impact the directionality of Rab11 vesicle transport
288 partially independent of its role in organizing microtubules in the constricting cells (Ko et al.,
289 2019).
290
291 **Rab11 reinforces apical AJs during apical constriction**
292 We next sought to determine the function of apically accumulated Rab11 vesicles. Single
293 plane fast imaging analysis revealed that Rab11 vesicles remained very dynamic after they
294 arrived at the cell apices, with a substantial fraction moving towards apical AJs (Figure 8A;
295 Video 5). The enrichment of Rab11 vesicles near AJs was particularly obvious during the
296 early stage of apical constriction when apical AJs had not yet formed a continuous belt and
297 appeared as discrete foci (Figure 8A). Intensity analysis of E-cadherin-GFP and Rab11-
298 mCherry along cell boundaries revealed a positive correlation between the two intensity
299 profiles (Figure 8B-D; Methods). As a control, similar analysis of Rab11 and a general
300 membrane marker P4M, a PI(4)P binding protein, showed no significant correlation (Figure
301 8B-D).
302
303 It remains unclear whether the targeting of Rab11 vesicles to the cell periphery is followed by

304 fusion of vesicles with the plasma membrane, as demonstrated in some other systems
305 (Grünfelder et al., 2003; Takahashi et al., 2012). We were not able to detect a clear, stable
306 plasma membrane-associated signal for YFP-Rab11. Interestingly, a constitutively active
307 form of Rab11 (Rab11CA), which is locked in its GTP-bound state, showed a prominent cell
308 membrane localization in addition to the vesicle form (Figure S3A, B). As another evidence
309 supporting the exocytic origin of the Rab11 vesicles, we found that injection of embryos with
310 Brefeldin A (BFA), an Arf GEF inhibitor commonly used to block trafficking out of ER-
311 Golgi system (Chardin and McCormick, 1999), resulted in rapid reduction of apical Rab11
312 vesicles and formation of large Rab11 aggregates between the cell apex and the nucleus
313 (Figure S3C).
314
315 The enrichment of Rab11 vesicles near the apical AJs prompted us to ask whether Rab11
316 vesicles regulate the structure and function of AJs. To address this question, we inhibited
317 Rab11 activity by injecting embryos with purified dominant negative Rab11 mutant proteins
318 (Rab11DN), an approach previously used to reveal the function of Rab11 in cellularization
319 (Pelissier et al., 2003). Rab11DN blocks the activation of endogenous Rab11 by binding to
320 and sequestering the guanine nucleotide exchange factors (GEFs) for Rab11 (Ullrich et al.,
321 1996). Importantly, the injection approach allowed stage-specific inhibition of Rab11, which
322 was critical for bypassing the requirement for Rab11 in pre-gastrulation stages (Pelissier et
323 al., 2003; Riggs et al., 2003; Tiwari and Roy, 2008). Injection of Rab11DN at mid/late
324 cellularization completely prevented the accumulation of apical Rab11 vesicles during apical

325 constriction (N = 5/5); whereas injection of Rab11DN close to the onset of apical constriction
326 either eliminated apically accumulated Rab11 vesicles (in 4.4 ± 1.3 min, N = 24/31; Figure
327 8E; Video 6) or decreased their number (N = 7/31). These results suggest that active Rab11 is
328 critical for both initiation and maintenance of apical accumulation of Rab11 vesicles. In
329 contrast, the size and morphology of perinuclear Rab11 compartments were not immediately
330 affected by injection (Figure 8E, green arrows). Injection of Rab11DN did not obviously
331 affect the formation or morphology of apical Rab35 tubules, which have been previously
332 implicated in facilitating endocytic membrane uptake from the apical domain during apical
333 constriction (Jewett et al., 2017; Miao et al., 2019; Figure S4). Strikingly, injection of
334 Rab11DN has a notable impact on the organization of apical AJs visualized by E-cadherin-
335 GFP. In the control GST-injected embryos, apical AJs became more continuous and belt-like
336 6 minutes into apical constriction. In contrast, Rab11DN-injected embryos showed more
337 fragmented apical AJs at comparable stage (Figure 8F). No difference was observed between
338 the control and Rab11DN- injected embryos at the lateral region of the cells where E-
339 cadherin is diffusely distributed (Figure 8F). Another apical AJ component, the Ajuba LIM
340 protein Jub (Razzell et al., 2018), showed reduced enrichment at AJs upon Rab11DN
341 injection (Figure 8G). Together, these results suggest that the apical Rab11 vesicles function
342 to reinforce apical AJs during apical constriction.
343
344 **Rab11 regulates Myosin II organization and promotes apical constriction**
345 Given the important role of AJs in the spatial organization of the supracellular actomyosin

346 network (Martin et al., 2010; Sawyer et al., 2009), we examined the dynamics and
347 organization of apical Myosin II in embryos injected with Rab11DN around the onset of
348 gastrulation. Rab11DN injection at this stage did not cause any obvious defect in the apical
349 activation of Myosin II (Figure 9A-C, GST vs. Rab11DN late injection). However,
350 quantification of the rate of myosin flow towards the ventral midline showed a significantly
351 lower rate in Rab11DN injected embryos compared to the control embryos (Figure 9D-G).
352 This defect indicates that Rab11DN injection impaired apical constriction, which we
353 confirmed by analysis of apical cell area changes (Figure S5A-E). The apical constriction
354 defect was associated with frequent breaks within the apical Myosin II network as well as the
355 underlying actin network (Figure 9H-J; Video 7). These myosin breaks occurred randomly
356 across the constriction domain and were usually promptly reconnected, which prevented the
357 complete tearing apart of the network. These observations suggest that the apical
358 accumulation of Rab11 vesicles is important for maintaining the structural integrity of the
359 apical actomyosin network. In support of this notion, similar myosin breaks have been
360 observed in various conditions when apical Rab11 vesicle accumulation was abolished,
361 such as disruption of microtubules (Ko et al.,2019), inhibition of dynein (Video 8) and BFA-
362 mediated block of exocytosis (Figure S3C, asterisks; Video 9).
363
364 Previous studies have demonstrated that apical constriction of the ventral mesodermal cells is
365 pulsed, with successive constriction pulses interrupted by pauses when cells stabilize their
366 constricted state ("ratcheting" mechanism; Martin et al., 2009; Mason et al., 2013). To ask

367 whether Rab11DN injection affects pulsed apical constriction, we analyzed the dynamics of
368 apical area change during ~ 4 – 6 minutes after the onset of apical constriction (Methods).
369 When Rab11 was inhibited, cells still exhibited pulsatile constriction behavior; there was no
370 significant difference in the pulse interval between Rab11DN and control GST injected
371 embryos (41.3 ± 17.8 s for GST injection, mean ± s.d., N = 21 cells from 2 embryos; 48 ±
372 20.4 s for Rab11DN injection, mean ± s.d., N = 26 cells from 2 embryos; Figure 10A-C).
373 However, Rab11DN injection resulted in an increased frequency of apical re-expansion after
374 constriction pulses (Figure 10D), indicating that the cells were less capable of stabilizing
375 their constricted state. Thus, the frequent myosin breaks caused by Rab11DN injection
376 impaired the stabilization of the constricted state during pulsed constriction.
377
378 The apical re-expansion events in Rab11DN injected embryos were usually associated with
379 visible local disconnection between the myosin structures and the cell-cell boundary (Figure
380 10E). During such events, apical AJs were often pulled to the opposite side from where
381 myosin breaks happened (Figure 10F, red arrows). These observations suggest that the
382 increased frequency of myosin breaks is due to impaired connections between junction and
383 the actomyosin network, perhaps as a consequence of altered junction organization. In line
384 with this view, we observed similar myosin breaks in embryos defective in *canoe*, the
385 *Drosophila* Afadin homolog that regulates the linkage of the actin cytoskeleton to AJs during
386 apical constriction (Video 10, Sawyer et al., 2009). Together, these results suggest that the
387 apical Rab11 vesicles function to reinforce AJs and thereby strengthen the anchorage of the

388 actomyosin network to the AJs. Interestingly, we found that myosin breaks and defect in
389 apical constriction in the Rab11DN-injected embryos were more prominent during later
390 phases of apical constriction (Video 7; Figure S5A-E), suggesting that the role of apical
391 Rab11 vesicles becomes more important as tissue tension increases.
392
393 In addition to myosin breaks, we observed a second phenotype in the spatial organization of
394 apical Myosin II. Instead of forming a supracellular meshwork with medioapically enriched
395 myosin foci connected by myosin fibers, Myosin II formed ring-like circular structure at the
396 apical domain of each constricting cell (Figure 9A). Interestingly, a recent study showed that
397 loss of anisotropy in apical tension led to similar myosin ring formation in the constricting
398 cells (Chanet et al., 2017). In Rab11DN-injected embryos, most myosin breaks
399 predominantly occurred in the anterior-posterior (AP) orientation (Figure 10G), which is the
400 direction in which tension is higher (Martin et al., 2010). These breaks may dissipate tension
401 in the AP direction, thereby reducing tension anisotropy of the actomyosin network and
402 causing myosin ring formation. In support of this view, the constricting cells in Rab11DN
403 injected embryos exhibited no obvious increase of anisotropy in their apical geometry at the
404 late stages of apical constriction, in sharp contrast to those in control embryos in which
405 anisotropy continued to increase during apical constriction (Figure S5F). These observations
406 led to an interesting hypothesis that the “myosin ring” phenotype in Rab11DN-injected
407 embryos is a consequence of increased frequency of breaks in the supracellular actomyosin
408 network.

409

410 **Distinct early and late functions of Rab11 in regulating apical Myosin II in mesoderm**

411 **primordium**

412 The lack of defects in apical myosin activation upon Rab11 inhibition apparently contradicted

413 with previous findings that Rab11 is required for apical myosin activation in several other

414 apical constriction-mediated tissue folding processes (Le and Chung, 2021; Ossipova et al.,

415 2014, 2015). In these studies, Rab11 was typically inhibited at a stage much earlier than the

416 onset of apical constriction. We found that injection of Rab11DN proteins during early

417 cellularization (> 30min before the onset of gastrulation) indeed resulted in a strong reduction

418 or lack of apical myosin accumulation during gastrulation (Figure 9A, B). Therefore, through

419 acute inhibition of Rab11, we were able to resolve the early and late functions of Rab11 in

420 apical constriction and identify a previously unappreciated function of Rab11 in the feedback

421 regulation of apical actomyosin network post Myosin II activation (Figure 10H).

422

423 ***Discussion:***

424 Our work reveals an intimate interplay between actomyosin network and Rab11-mediated
425 vesicular trafficking during apical constriction mediated epithelial folding. Combining live
426 imaging with genetic, optogenetic and pharmacological approaches, we show that during
427 ventral furrow formation, apical actomyosin induces dynein- and microtubule-dependent,
428 biased transport of Rab11 vesicles towards the cell apices, which facilitates the enrichment of
429 the vesicles at apical AJs. By acute elimination of apical Rab11 vesicles through Rab11DN
430 injection, we further present evidence that these vesicles are important for maintaining the
431 structural integrity of the AJs and for preventing undesired breaks between actomyosin
432 network and the AJs during apical constriction. These results suggest an actomyosin-
433 dependent, Rab11-mediated feedback mechanism that serves to reinforce the connections
434 between the actomyosin network and apical AJs (Figure 10H). In further support of the
435 proposed mechanism, we found that acute disruption of Rab11 vesicle transport or blocking
436 trafficking through the Golgi apparatus resulted in similar defects in the integrity of the
437 supracellular actomyosin network. Finally, we show that this feedback mechanism is separate
438 from the function of Rab11 in promoting apical Myosin II activation as previously reported in
439 other systems. The mechanism identified in this work allows the tissue to promptly adapt to
440 the increased tissue tension during apical constriction and maintain the integrity of the force
441 generation machinery in the process of tissue folding.

442

443 The apical enrichment of Rab11 vesicles is closely associated with the formation of intact

444 actomyosin network at the apical domain of the cell, as evidenced by the strict correlation
445 between the two processes in a variety of conditions we tested. In particular, we show that
446 accumulation of myosin at the apical cortex without F-actin (and thereby lacking
447 contractility) is not sufficient to induce vesicle accumulation, and that the directional bias in
448 Rab11 vesicle transport diminishes immediately after acute actomyosin inactivation. The
449 outcomes of these tests also let us rule out the requirement of actomyosin-AJ coupling and
450 apical shrinking for Rab11 vesicle accumulation. Since actomyosin networks are intrinsically
451 contractile, our findings raise an intriguing possibility that the biased Rab11 vesicle transport
452 is subjected to mechanosensitive regulations. In recent years, it has been increasingly
453 appreciated that cell and tissue-scale mechanical forces can impact intracellular membrane
454 trafficking. For example, high membrane tension can suppress the formation of endocytic
455 vesicles (Wu et al., 2017) and promote vesicle fusion with lipid bilayer (Shillcock and
456 Lipowsky, 2005; Staykova et al., 2011). Mechanical stresses can also impact vesicle transport
457 and distribution in neurons (Ahmed and Saif, 2014; Ahmed et al., 2012; Siechen et al., 2009)
458 and trigger regulated exocytosis in various contexts (Boycott et al., 2013; Gauthier et al.,
459 2011; Khandelwal et al., 2013). The rapid alteration in Rab11 vesicle transport in response to
460 actomyosin activities provides a potential example of mechanical regulation of intracellular
461 trafficking in the context of tissue morphogenesis.
462
463 The way how apical constriction affect Rab11 vesicle transport is unknown. Apical
464 constriction may cause changes in the activity of the motor complexes that drive the motion

465 of Rab11 vesicles. Regulation of dynein-mediated transport can occur at multiple levels,
466 including Rab11-adaptor binding, adaptor activities, adaptor-motor binding, dynein
467 recruitment to microtubules, and motor activity itself (Dillman and Pfister, 1994; Fu and
468 Holzbaur, 2013; Horgan et al., 2010; Moughamian et al., 2013; Otani et al., 2011; Vaughan et
469 al., 2002; Wang et al., 2019). Alternatively, apical actomyosin contractions may bias the
470 direction of transport by generating a "sink" that retains the vesicles at the apical side,
471 thereby inhibiting the initiation of the reverse, basally directed transport of the vesicles.
472 Future research is required to further tease apart these possibilities.
473
474 Another important question remained to be address is the molecular basis of the myosin
475 breaks observed in Rab11DN injected embryos. Rab11 may regulate apical constriction by
476 regulating endocytic recycling of Fog and GPCR (Fuse et al., 2013; Jha et al., 2018; Pouille
477 et al., 2009). However, alteration in Fog-GPCR signaling would be expected to affect apical
478 myosin II activation, which was not observed in our experiments upon acute Rab11DN
479 injection. Rab11 may also be involved in Rab35-mediated endocytosis of apical membrane,
480 which has been shown to facilitate ratcheted constriction (Jewett et al., 2017; Miao et al.,
481 2019). However, we found that the apical Rab11 vesicles are not derived from endocytosis
482 and that acute injection of Rab11DN did not obviously affect the Rab35 compartments.
483 Instead, we show that in Rab11DN injected embryos, the appearance of frequent myosin
484 breaks was associated with severe fragmentation of apical AJs, raising the possibility that the
485 function of Rab11 in maintaining the integrity of the actomyosin network is attributed to its

role in regulating apical AJs. Rab11 recycling endosomes have been shown to regulate the delivery of E-cadherin to the AJs in a number of other cell and tissue contexts (Langevin et al., 2005; Le Droguen et al., 2015; Lock and Stow, 2005; Woichansky et al., 2016; Yashiro et al., 2014). However, we did not detect E-cadherin-GFP signal on Rab11 vesicles during apical constriction. It is possible that the signal was too weak to be detected by the method we used. Alternatively, these vesicles may function to transport other junction components or regulators. Finally, Rab11 vesicles may regulate the connection between AJ and actomyosin network by delivering actin regulators to AJs, as dynamic actin turnover at AJs has been shown to impact the detachment and reattachment of actomyosin network to AJs (Jodoin et al., 2015). Future studies identifying the cargos of the Rab11 vesicles during apical constriction will be the key to understand the molecular function of these vesicles.

498 ***Materials and methods:***

499 **Fly stocks and genetics**

500 *Drosophila melanogaster* flies were grown and maintained at 18°C and crosses were raised
501 and maintained at room temperature (21 – 23°C) unless otherwise mentioned. All flies were
502 raised on standard fly food. For embryo collection, flies with corresponding genotype were
503 used to set up cages and maintained at 18°C, and embryos were collected from apple juice
504 agar plate containing fresh yeast paste.

505

506 For most experiments, embryos expressing endogenously tagged YFP::Rab11 (Dunst et al.,
507 2015) (BDSC Stock#62549) were imaged to visualize Rab11 vesicles. We also generated
508 UAS-mCherry::Rab11 transgenic flies for dual-color imaging with other GFP-tagged markers
509 (Figure 6A and B, Figure 8A, Figure S2C and Figure S4). For lines with UAS-driven
510 transgenes or shRNA, we used GAL4 driver lines carrying matα4-GAL-VP16 (denoted as
511 "mat67" on the 2nd chromosome and "mat15" on the 3rd chromosome) to drive maternal
512 expression in the embryo through either direct cross or recombination.

513

514 The following fly lines were generated for dual-color imaging of Rab11 with other markers in
515 this study:

516 – Sqh::mCherry; YFP::Rab11
517 – Gap43::mCherry/Cyo; YFP::Rab11
518 – mat67 mCherry::Rab11; mat15 GFP::Jupiter

519 – mat67 mCherry::Rab11; mat15 E-cadherin::GFP

520 – mat67 mCherry::Rab11;mat15 mCherry::P4M

521

522 Figure S1: To examine other organelle behavior during apical constriction, the following lines

523 were either directly used or first crossed to mat67; mat15 flies in order to obtain embryos

524 expressing the corresponding fluorescent marker:

525 – UAS-Arf79F::GFP (BDSC Stock#65850)

526 – UAS-KDEL::GFP (BDSC Stock#9898)

527 – UAS-YFP::Rab7 (BDSC Stock#23641)

528 – YFP::Rab5 (BDSC Stock#62543)

529 – YFP::Rab8 (BDSC Stock#62546)

530

531 Figure 2C: To knock down Myosin II, female flies of a TRiP *zipper*; YFP::Rab11 stock

532 generated from a TRiP *zipper* RNAi line (BDSC Stock#37480) were crossed to male flies

533 from stock mat67 Sqh::mCherry; mat15 YFP::Rab11 to obtain F1 TRiP *zipper*/mat67

534 Sqh::mCherry; YFP::Rab11/mat15 YFP::Rab11 flies, and embryos from these F1 flies were

535 collected for imaging.

536

537 Figure 2D: To generate ventralized embryos, *Spn27A1*/Cyo; Sqh::mCherry YFP::Rab11/TM3

538 was crossed to Df(2L)BSC7/Cyo; Sqh::mCherry YFP::Rab11/TM3 to obtain *Spn27A1*/

539 Df(2L)BSC7; Sqh::mCherry YFP::Rab11 flies, and embryos from these flies were collected

540 for imaging. *Spn27A* encodes a serine protease inhibitor that regulates dorsal-ventral
541 patterning in early embryos by inhibiting the Toll-Dorsal pathway (Ligoxygakis et al., 2003).
542 Consistent with previous reports, *Spn27A* mutant embryos showed a ventralized phenotype
543 with expanded apical Myosin II activation domain during gastrulation (Figure 2D;
544 Ligoxygakis et al., 2003).
545
546 Figure 3C: To knock down α-catenin, female flies of TRiP *α-catenin* RNAi line (BDSC
547 Stock# 33430) were crossed to male flies from stock mat67 Sqh::mCherry; mat15
548 YFP::Rab11 to obtain F1 +/mat67 Sqh::mCherry; TRiP *α-catenin* /mat15 YFP::Rab11 flies,
549 and embryos from these F1 flies were collected for imaging. Consistent with previous
550 reports, disrupting AJs did not prevent apical myosin activation, but rather impaired the
551 connection between the actomyosin network and the cell-cell boundaries. As a result, Myosin
552 II coalesced into concentrated spots at the center of each individual medioapical domain
553 (Martin et al., 2010).
554
555 Figure 4A-C: To overexpress Fog, female flies from UAS-Fog stock were crossed to male
556 flies from stock mat67 Sqh::mCherry; mat15 E-cad::GFP or mat67 Sqh::mCherry;
557 YFP::Rab11 to obtain corresponding F1 flies, and embryos from these F1 flies were collected
558 for imaging. As shown in a previous study, ectopic myosin activation in dorsal cells by
559 ectopic expression of Fog does not cause cell apex shrinking or tissue indentation, thereby
560 providing a scenario where actomyosin contractility and apical cell area reduction is

561 decoupled (Morize et al., 1998).

562

563 Figure 7A-F: Female flies from stock CRY2::mCherry::Rho1DN YFP::Rab11/TM6C;

564 CIBNpm/FM7 were crossed to male flies from stock mat67 Sqh::mCherry; mat15

565 YFP::Rab11 to generate mat67 Sqh::mCherry/+; CRY2::mCherry::Rho1DN

566 YFP::Rab11/mat15 YFP::Rab11; CIBNpm/+ flies, and embryos from these flies were

567 collected for imaging.

568

569 Figure 7G, H: Female flies from stock CRY2::mCherry::Rho1DN /TM6C; CIBNpm/FM7

570 were crossed to male flies from stock mat67 Sqh::mCherry; mat15 GFP::Jupiter to generate

571 mat67 Sqh::mCherry/+; CRY2::mCherry::Rho1DN / mat15 GFP::Jupiter; CIBNpm/+ flies,

572 and embryos from these flies were collected for imaging.

573

574 Figure 8, 10, S5: Sqh::mCherry E-cadherin::GFP was used for Rab11DN injection

575 experiment for examining adherens junction phenotype and quantifying apical area change.

576 Sqh::mCherry mat67; mat15 UAS-Jub::GFP was used for figure 8G.

577

578 Figure 9A-H: embryos from SqhmCherry; YFP-Rab11 flies were used.

579

580 Figure 9I: embryos from mat67 Sqh::mCherry; mat15 UtrABD::GFP were used in Rab11DN

581 injection experiment for examining apical actin network.

582

583 Figure S2C: embryos from mat67 mCherry::Rab11/YFP::Rab5 flies were used.

584

585 Figure S2D, E: The fly stock used for temperature shift experiment is *shi*^{ts}/ *shi*^{ts};

586 Sqh::mCherry; YFP::Rab11.

587

588 Figure S3A, B: To visualize the localization of constitutively active Rab11, UAS-

589 YFP::Rab11Q70L (BDSC Stock#9791) was crossed to mat67; mat15 males, and embryos

590 from F1 females were used for imaging.

591

592 Figure S4: embryos from mat67 mCherry::Rab11/UAS-YFP::Rab35 were used.

593

594 Video 10: A TRiP *canoe* RNAi line (BDSC Stock#38194) was used for *canoe* knockdown.

595 Female flies from the TRiP *canoe* stock were crossed to male flies from stock mat67

596 Sqh::mCherry; mat15 E-cad::GFP to obtain F1 TRiP *canoe*/mat67 Sqh::mCherry; +/mat15 E-

597 cad::GFP flies, and embryos from these F1 flies were collected for imaging.

598

599 **Molecular cloning and generation of transgenic fly lines**

600 To make construct for in vitro expression of recombinant dominant negative Rab11 (S25N)

601 protein, dominant negative Rab11 coding sequence was PCR amplified from genomic DNA

602 of UAS-YFPRab11DN (BDSC Stock#9792) and inserted into pGEX-6p-1 vector (a gift from

603 the Griffin lab, Dartmouth College) using BamHI and XhoI restriction sites.

604

605 To make constructs for transgenic fly lines, mCherry-P4M double strand DNA was

606 synthesized in vitro (Integrated DNA Technologies) and inserted into a fly transformation

607 vector (pTiger, courtesy of S. Ferguson, State University of New York at Fredonia, Fredonia,

608 NY, USA) using NotI and NheI restriction site to generate the pTiger-mCherry-P4M plasmid.

609

610 To make pTiger-mCherry-Rab11 construct, wild type Rab11 coding sequence was PCR

611 amplified from genomic DNA of UAS-YFP::Rab11 (BDSC Stock# 9790) and cloned into

612 pTiger-mCherry-P4M construct using SpeI and NheI restriction sites to replace the P4M

613 sequence.

614

615 The resulting pTiger-mCherry-P4M and pTiger-mCherry-Rab11 constructs were sent to

616 BestGene, Inc., for integration into either attP2 or attP40 site using the phiC31 integrase

617 system (Groth et al., 2004).

618

619 **Live imaging and optogenetics**

620 Embryos were dechorionated in 3% bleach, rinsed with water 12 times and mounted in water

621 in a 35 mm MatTek glass-bottom dish (MatTek Corporation). Unless otherwise mentioned,

622 all images were obtained using a Nikon inverted spinning disk confocal microscope equipped

623 with the perfect focus system and Andor W1 dual camera, dual spinning disk module. An CFI

624 Plan Apo Lambda 60×/1.40 WD 0.13 mm Oil Objective Lens objective was used for imaging
625 at room temperature. YFP and GFP tagged proteins were imaged with a 488-nm laser and
626 mCherry tagged proteins were imaged with a 561-nm laser. Images in Figure 1A, S1A and B
627 were obtained using an upright Olympus FV-MPERS multiphoton microscope equipped with
628 the InSight Deep Laser System with an Olympus 25X/1.05 water dipping objective
629 (XLPLN25×WMP2). Images in Figure 1D, 2A, 2D, S2, S3 were obtained using a Zeiss Axio
630 Observer laser scanning confocal microscope (LSM 880).
631
632 For optogenetic experiments, flies were kept in the dark and live sample preparation was
633 performed under red light. Embryos were first imaged with 561-nm laser to visualize Myosin
634 II signal to determine the developmental stage of the embryo. Once the embryo reached the
635 desired stage, two-color imaging with both 488-nm and 561-nm lasers were carried out,
636 where the 488-nm laser was used for both optogenetic stimulation and YFP-Rab11
637 visualization. The Opto-Rho1DN optogenetic tool used in this experiment is based on the
638 CIBN-CRY2 system (Guglielmi et al., 2015; Kennedy et al., 2010). Blue-light dependent
639 recruitment of a CRY2-Rho1DN fusion protein to plasma membrane-anchored CIBN blocks
640 activation of endogenous Rho1, causing rapid dissociation of Myosin II and F-actin from the
641 cell apices, thereby acutely inhibits apical actomyosin contractility (Guo et al., 2021).
642
643 For the temperature shift experiment with shi^{ts} mutants, a Zeiss Axio Observer laser scanning
644 confocal microscope (LSM 880) with an incubation chamber was used. Embryos subjected to

645 restrictive temperature were prepared at room temperature and then transferred to an
646 incubation chamber, which was preheated to 32°C. A 40X/1.3 numerical aperture oil-
647 immersion objective, and 488-nm argon laser and 561-nm laser were used for imaging.
648

649 **Rab11 dominant negative protein expression and purification**

650 pGEX-6p-1-Rab11DN plasmid was transformed into E.coli (BL21(DE3), New England
651 BioLabs). An empty vector with only GST coding sequence was also transformed as control.
652 After IPTG induction, bacteria were resuspended in 32 mL lysis buffer (50 mM Tris pH7.5,
653 150 mM NaCl, 0.1% Triton X-100, 1 mM PMSF, 1 mM DTT) and lysed with 0.25 mg/mL
654 lysozyme incubation on ice for 2 h followed by sonication (6 rounds of 10 pulses every 1
655 minute). GST and GST-Rab11DN were purified from the supernatant with Glutathione
656 Sepharose 4B GST-tagged protein purification resin (GE17-0756-01, Sigma-Aldrich) using
657 batch method. Eluted protein was dialyzed using slide-A-Lyzer dialysis cassettes (Cat#66380,
658 Thermo Scientific) with 50 mM Tris buffer (pH8.0) and further concentrated to a final
659 concentration of ~200 μM with Amicon Ultra-0.5mL centrifugal filters (Cat#UFC501024,
660 Millipore Sigma).
661

662 **On-stage drug / protein injection**

663 Embryos at cellularization stage were prepared as previously described, then mounted ventral
664 side down on a 50 x 25 mm glass coverslip pre-covered with a thin layer of glue. Embryos
665 were dried for 10-15 minutes in a desiccator. Embryos were then covered with halocarbon oil

666 (halocarbon 700/halocarbon 27 = 3:1). A homemade injection device mounted next to the
667 spinning disk confocal microscope was used for on-stage injection. Embryos were injected
668 laterally into the ventral part of the embryo. 50 mM Y-27632 (Enzo Life Sciences), 25
669 mg/mL colchicine (Sigma-Aldrich), 5 mg/mL Cytochalasin D (Sigma-Aldrich), 0.5 μg/μL
670 FM4-64 (Invitrogen^{TM}) and 10 mg/mL Brefeldin A (Sigma-Aldrich) were used for
671 corresponding experiment. For Rab11DN injection, Triton X-100 was added to a final
672 concentration of 0.1% to prevent the solution from clogging the needle. For dynein and GST
673 antibody injection, commercial monoclonal antibodies against cytoplasmic dynein
674 intermediate chain (Cat#sc-13524, Santa Cruz Biotechnology) and monoclonal antibody
675 against GST (Cat#sc-138, Santa Cruz Biotechnology) were first concentrated to 2 mg/mL
676 with Amicon Ultra-0.5 mL centrifugal filters before injection (Cat#UFC501024, Millipore
677 Sigma). For FM4-64 injection, the membrane dye was injected into the perivitelline space at
678 late cellularization to label the cell membrane and monitor the localization of endocytosed
679 membrane dye. For all other injections, the indicated reagents were injected into the embryo.
680

681 **Image processing and analysis**

682 All images were processed using ImageJ (NIH) and MATLAB (MathWorks). For the
683 following figures, due to laser power fluctuation and the extent of photobleaching with
684 different imaging duration, the contrast was adjusted to make the cytoplasmic signal
685 comparable: Figure 2A, 2B (Rab11), 2C (Myosin II), 2D (Myosin II and Rab11), S3(Myosin
686 II and Rab11), 6C (Rab11), 6H (Myosin II and Rab11), 8E, 8F, 9A.

687

688 For 3D segmentation and rendering of Rab11-positive structures (Figure 1F-H), we first
689 segmented a group of presumptive mesodermal cells in membrane channel using Embryo
690 Development Geometry Explorer (EDGE), a MATLAB-based software (Gelbart et al., 2012)
691 to generate individual cell mask. Then we used ilastik, a machine learning based software
692 (Berg et al., 2019) to segment Rab11 vesicles and perinuclear compartments in the Rab11
693 channel (Pixel classification) to generate a probability map. A custom MATLAB script was
694 used to convert the probability map for vesicle and perinuclear compartment to binary mask.
695 These masks were applied to original image to remove background signal and 3D rendering
696 of resulting images was created using Nikon Elements software. To generate 3D view of
697 Rab11 structures in a single cell, the cell mask generated from EDGE was applied to the
698 processed Rab11 images before 3D rendering. In Figure 1F and 1G, the original images are
699 generated by maximum intensity projection rendering method while the rest of images are
700 generated with alpha blending method.

701

702 For vesicle tracking in embryos expressing YFP-Rab11 and mCherry-Sqh (Figure 5A-E,
703 Figure 7A-E), a 13.8 μm x 6.9 μm region of interest including approximately one constricting
704 cell at 50% egg length was selected, and Rab11 vesicles were manually marked frame by
705 frame for each trajectory using a multi-point tool in ImageJ. The x-y coordinates of
706 individual vesicles over time were then exported. A MATLAB script was written to
707 reconstruct the trajectories based on the coordinate information. The direction of each

708 trajectory was defined by the relative translocation of the vesicle along apical basal axis
709 between trackable start and end positions. All trajectories were grouped into two categories
710 based on their direction (apical or basal) for further analysis of parameters, including
711 trajectory count, average velocity, trajectory length and trajectory duration.
712
713 To validate the vesicle tracking analysis (Figure 5F, G), we performed the following analyses.
714 First, we imaged embryos expressing both myosin and membrane markers at multiple z-
715 planes. This approach allowed us to map the position of the single plane image to the cross-
716 section view of the embryo (Figure 5F). The results confirmed that our single-plane imaging
717 approach captured the cells located at the medial-lateral boundaries of the constricting
718 domain. We noticed that although all of these cells showed apical myosin accumulation,
719 some cells were constricted apically, whereas others appeared to be in the process of apical
720 constriction or even stretched by the more centrally localized constricting cells. These
721 observations were consistent with a recent report demonstrating that apical myosin
722 contractility is graded from the center of the constriction domain (Denk-Lobnig et al., 2021).
723 Second, we imaged embryos expressing both a membrane marker and mCherry-Rab11
724 (overexpression) and quantified transport events only in cells displaying obvious apical
725 shrinking. We found no significant difference between the results from the original and the
726 new analyses (Figure 5G). These additional analyses also indicate that apical actomyosin
727 accumulation, but not apical area reduction, is the determining factor for the biased transport
728 of Rab11 vesicles, consistent with the observation in dorsal cells with ectopic Fog expression

729 (Figure 4A-C).

730

731 For quantification of vesicle density in 2D (Figure 4D-F), 3 separate ROIs covering most of
732 the constriction region were selected, with each ROI enclosing a relatively flat piece of tissue
733 surface (based on the apical Myosin II signal). For each ROI, a Z position near the apical
734 surface where most vesicles were accumulated was selected for quantification. Vesicles were
735 detected using the Find Maxima function in ImageJ in combination with manual correction to
736 ensure accuracy of the counting. For vesicle counting in 3D (Figure 4D-F), the FIJI plugin
737 3D Maxima Finder was used and the noise tolerance parameter was determined based on
738 average intensity of the entire image stack (Ollion et al., 2013).

739

740 The colocalization between Rab11-mCherry and E-cadherin-GFP (Figure 8B-D) was
741 quantified in embryos at the stage of early ventral furrow formation. For each embryo, 5 non-
742 neighboring constricting cells were manually segmented using a multi-point tool to mark the
743 vertices of the cell outline. A MATLAB script was written to import the coordinates of these
744 vertices to create the cell outline. For each cell outline, a series of closely spaced and evenly
745 distributed sampling points were generated along the outline. For each sampling point, E-
746 cadherin-GFP signal intensity on that single pixel was extracted as the junction signal, and
747 average Rab11-mCherry signal intensity within a radius of 5 pixels (~0.54 μm) was
748 calculated as Rab11 signal for the same point. For each cell, a scatter plot of E-cadherin
749 intensity over Rab11 intensity for all the sampling points was generated, and a correlation

750 coefficient was calculated. A similar analysis was performed between P4M-GFP and Rab11-
751 mCherry as a control.
752
753 For Myosin II intensity quantification (Figure 9B), 100-pixel by 100-pixel ROIs (10.8 μm X
754 10.8 μm) were taken from the apical Myosin II domain. Average intensity R was measured
755 inside the ROI on that plane, and background noise at the same plane (R_{bg}) was measured as
756 the mean intensity of a random ROI outside the embryo. To assess cytoplasmic myosin
757 intensity (C), we used the same ROI position but at a slightly deeper Z below the apical
758 myosin network, the background noise at that plane (C_{bg}) was measured as described above.
759 The normalized Myosin II intensity $I = (R-R_{bg}) / (C-C_{bg})$. Embryos at ~6 – 7 min after the
760 onset of gastrulation were used for quantification.
761
762 To quantify the rate of apical constriction based on the movement of apical Myosin II
763 structures (Figure 9D-G), kymographs were generated from the same dataset of the above-
764 mentioned 100-sec myosin movies. For each embryo, a series of myosin kymographs were
765 generated by average projection over every 30 pixels (3.2 μm) along anterior posterior axis.
766 Bandpass filter in ImageJ were used to remove noise. A custom MATLAB script was used for
767 automatic segmentation of individual myosin traces and fitting with lines. Rate of Myosin II
768 moving towards ventral midline was extracted by calculating the slope of each myosin trace.
769 Velocity of Myosin II at ventral midline was subtracted to correct for the drift of ventral
770 midline itself. The rate of myosin movement was then plotted against the distance of the

771 corresponding myosin structure to ventral midline at the time when tracing started.

772

773 For quantification of myosin breaks (Figure 9J, 10G), a maximum projection over 3 – 5 μm
774 thick Z stacks that include all apical Myosin II signal was generated. A ~100-sec time
775 window starting from the time point when the Myosin II domain at the ventral surface
776 exhibits a relatively clear domain boundary (~6 – 7 min after the onset of gastrulation) was
777 selected to count the number of myosin break events. At the site where myosin break occurs,
778 the myosin fiber usually snaps and the two ends rapidly retract, which creates a clear gap
779 between neighboring myosin clusters.

780

781 To analyze the cell area dynamic from fast movies (Figure 10A-D), the time lapse movie of a
782 subapical single slice from E-cad channel was first rearranged to convert T dimension into Z
783 dimension. Individual cells in the resulting image were segmented in ilastik using carving
784 method (Berg et al., 2019). Once segmented, cell area, constriction rate and pulse duration
785 were calculated using a customized MATLAB script. In order to find the peaks for the
786 constriction rate, the constriction rate curve was first smoothed using MATLAB smooth
787 function with a span of 5. The rate was then inverted to convert valleys into peaks and
788 MATLAB findpeaks function was used to locate the peaks and pulse duration was calculated
789 as the interval between neighboring peaks.

790

791 To quantify the rate of apical constriction from E-cadherin-GFP movies (Figure S5A, B),

792 images at 6 – 7 μm below the apical surface were used to measure the cell area change over
793 time. A group of constricting cells at the ventral most region of the embryo were outlined
794 frame by frame using multi-point tool in ImageJ. The area of the same cell group over time
795 was then calculated and plotted using MATLAB.
796
797 To analyze the distribution of cell area in the same embryo at 2 min, 5 min and 8 min after
798 onset of gastrulation (Figure S5C-E), individual constricting cell was segmented using
799 Embryo Development Geometry Explorer (EDGE), a MATLAB-based software (Gelbart et
800 al., 2012). Individual cell area was then calculated, and the distribution histogram of cell area
801 was plotted. Cell anisotropy was calculated based on the same segmented cell dataset (Figure
802 S5F). Two orthogonal (anteroposterior and mediolateral) lines passing the centroid of the cell
803 were drawn across the segmented cell, and the cell anisotropy was calculated as the ratio
804 between the anteroposterior intercept by the cell boundary and the mediolateral intercept.
805
806 **Statistics**
807 Statistical comparisons were performed using two tailed one-sample t test or two-tailed
808 Student's t tests. Sample sizes can be found in figure legends. *p* values were calculated using
809 MATLAB ttest (Two tailed one-sample t test) and ttest2 function (Two tailed Student's t test).
810
811 **Supplemental Material**

812 Figure S1 shows changes in 3D Rab11 structures during ventral furrow formation as well as a
813 comparison to other endomembrane compartments. Figure S2 shows that Rab11 vesicles are
814 not derived from endocytosis. Figure S3 shows the localization of constitutively active Rab11
815 during ventral furrow formation and the impact of BFA injection on Rab11 and Myosin II.
816 Figure S4 shows that Rab11DN injection does not obviously affect Rab35 structures. Figure
817 S5 shows that acute inhibition of Rab11 results in reduced rate of apical constriction. Video 1
818 shows myosin network relaxation immediately after cytoD injection. Video 2 shows Rab5,
819 Rab11 localization relative to endocytosed vesicles after FM4-64 membrane dye injection.
820 Video 3 shows the impact of acute disruption of MTs on Rab11 vesicle transport. Video 4
821 shows the impact of dynein inhibition on Rab11 vesicle transport. Video 5 shows the
822 dynamics of Rab11 vesicles near apical adherens junctions. Video 6 shows the rapid
823 disappearance of Rab11 vesicles after Rab11DN injection. Video 7 shows that injection of
824 Rab11DN causes frequent breaks within the apical actomyosin network. Video 8 shows that
825 injection of dynein antibody affects apical Rab11 vesicle accumulation and causes frequent
826 myosin breaks. Video 9 shows that injection of BFA results in abnormal Rab11 structures and
827 causes frequent myosin breaks. Video 10 shows that knockdown of Canoe causes frequent
828 myosin breaks.
829

830 ***Acknowledgments:***

831 We thank members of the He lab and the Griffin lab for discussions throughout this work;
832 Yashi Ahmed, Charles K.Barlowe and Adam Martin for valuable comments on the
833 manuscript; Ann Lavanway and Zednek Svindrych for technical support with imaging;
834 Robert Robertson for help with on-stage injection setup. We thank the Wieschaus lab and the
835 De Renzis lab for sharing reagents. We thank the Bloomington *Drosophila* Stock Center for
836 fly stocks. This study was supported by NIGMS ESI-MIRA R35GM128745 and American
837 Cancer Society Institutional Research Grant #IRG –82-003-33 to B.H. The study used core
838 services supported by STANTO15R0 (CFF RDP), P30-DK117469 (NIDDK P30/DartCF),
839 and P20-GM113132 (bioMT COBRE).

840

841 ***Author Contributions:***

842 W.C. and B.H. designed the study. W.C. performed the experiments and analyzed the data.
843 W.C. and B.H. wrote the manuscript.

844

845 ***Declaration of Interests:***

846 The authors declare no competing interests.

847

848 ***References:***

849 Ahmed, W.W., and Saif, T.A. (2014). Active transport of vesicles in neurons is modulated by
850 mechanical tension. Scientific Reports *4*, 4481.

851 Ahmed, W.W., Li, T.C., Rubakhin, S.S., Chiba, A., Sweedler, J.V., and Saif, T.A. (2012).
852 Mechanical Tension Modulates Local and Global Vesicle Dynamics in Neurons. Cel. Mol.
853 Bioeng. *5*, 155–164.

854 Amano, M., Ito, M., Kimura, K., Fukata, Y., Chihara, K., Nakano, T., Matsuura, Y., and
855 Kaibuchi, K. (1996). Phosphorylation and Activation of Myosin by Rho-associated Kinase
856 (Rho-kinase)*. Journal of Biological Chemistry *271*, 20246–20249.

857 Benli, M., Döring, F., Robinson, D.G., Yang, X., and Gallwitz, D. (1996). Two GTPase
858 isoforms, Ypt31p and Ypt32p, are essential for Golgi function in yeast. The EMBO Journal *15*,
859 6460–6475.

860 Berg, S., Kutra, D., Kroeger, T., Straehle, C.N., Kausler, B.X., Haubold, C., Schiegg, M., Ales,
861 J., Beier, T., Rudy, M., et al. (2019). ilastik: interactive machine learning for (bio)image
862 analysis. Nat Methods *16*, 1226–1232.

863 van der Bliek, A.M., and Meyerowrtz, E.M. (1991). Dynamin-like protein encoded by the
864 Drosophila shibire gene associated with vesicular traffic. Nature *351*, 411–414.

865 Boycott, H.E., Barbier, C.S.M., Eichel, C.A., Costa, K.D., Martins, R.P., Louault, F., Dilanian,
866 G., Coulombe, A., Hatem, S.N., and Balse, E. (2013). Shear stress triggers insertion of voltage-
867 gated potassium channels from intracellular compartments in atrial myocytes. Proceedings of
868 the National Academy of Sciences *110*, E3955–E3964.

869 Chanet, S., Miller, C.J., Vaishnav, E.D., Ermentrout, B., Davidson, L.A., and Martin, A.C.
870 (2017). Actomyosin meshwork mechanosensing enables tissue shape to orient cell force. Nat
871 Commun *8*.

872 Chardin, P., and McCormick, F. (1999). Brefeldin A: The Advantage of Being Uncompetitive.
873 Cell *97*, 153–155.

874 Chen, W., Feng, Y., Chen, D., and Wandinger-Ness, A. (1998). Rab11 Is Required for Trans-
875 Golgi Network–to–Plasma Membrane Transport and a Preferential Target for GDP
876 Dissociation Inhibitor. Mol Biol Cell *9*, 3241–3257.

877 Collinet, C., and Lecuit, T. (2021). Programmed and self-organized flow of information during
878 morphogenesis. Nature Reviews Molecular Cell Biology 1–21.

879 Coravos, J.S., and Martin, A.C. (2016). Apical Sarcomere-like Actomyosin Contracts
880 Nonmuscle Drosophila Epithelial Cells. Developmental Cell *39*, 346–358.

881 Dawes-Hoang, R.E., Parmar, K.M., Christiansen, A.E., Phelps, C.B., Brand, A.H., and
882 Wieschaus, E.F. (2005). folded gastrulation, cell shape change and the control of myosin
883 localization. Development *132*, 4165–4178.

884 Denk-Lobnig, M., Totz, J.F., Heer, N.C., Dunkel, J., and Martin, A.C. (2021). Combinatorial
885 patterns of graded RhoA activation and uniform F-actin depletion promote tissue curvature.
886 Development *148*, dev199232.

887 Dillman, J.F., and Pfister, K.K. (1994). Differential phosphorylation in vivo of cytoplasmic
888 dynein associated with anterogradely moving organelles. J Cell Biol *127*, 1671–1681.

889 Dunst, S., Kazimiers, T., von Zadow, F., Jambor, H., Sagner, A., Brankatschk, B., Mahmoud,
890 A., Spannl, S., Tomancak, P., Eaton, S., et al. (2015). Endogenously Tagged Rab Proteins: A
891 Resource to Study Membrane Trafficking in Drosophila. Developmental Cell *33*, 351–365.

892 Fletcher, D.A., and Mullins, R.D. (2010). Cell mechanics and the cytoskeleton. Nature *463*,
893 485–492.

894 Fu, M., and Holzbaur, E.L.F. (2013). JIP1 regulates the directionality of APP axonal transport
895 by coordinating kinesin and dynein motors. J Cell Biol *202*, 495–508.

896 Fuse, N., Yu, F., and Hirose, S. (2013). Gprk2 adjusts Fog signaling to organize cell movements
897 in Drosophila gastrulation. Development *140*, 4246–4255.

898 Gauthier, N.C., Fardin, M.A., Roca-Cusachs, P., and Sheetz, M.P. (2011). Temporary increase
899 in plasma membrane tension coordinates the activation of exocytosis and contraction during
900 cell spreading. Proceedings of the National Academy of Sciences *108*, 14467–14472.

901 Gelbart, M.A., He, B., Martin, A.C., Thiberge, S.Y., Wieschaus, E.F., and Kaschube, M. (2012).
902 Volume conservation principle involved in cell lengthening and nucleus movement during
903 tissue morphogenesis. Proceedings of the National Academy of Sciences *109*, 19298–19303.

904 Gheisari, E., Aakhte, M., and Müller, H.-A.J. (2020). Gastrulation in Drosophila melanogaster:
905 Genetic control, cellular basis and biomechanics. Mechanisms of Development *163*, 103629.

906 Gilmour, D., Rembold, M., and Leptin, M. (2017). From morphogen to morphogenesis and
907 back. Nature *541*, 311–320.

908 Groth, A.C., Fish, M., Nusse, R., and Calos, M.P. (2004). Construction of Transgenic
909 Drosophila by Using the Site-Specific Integrase From Phage φC31. Genetics *166*, 1775–1782.

910 Grünfelder, C.G., Engstler, M., Weise, F., Schwarz, H., Stierhof, Y.-D., Morgan, G.W., Field,
911 M.C., and Overath, P. (2003). Endocytosis of a Glycosylphosphatidylinositol-anchored Protein
912 via Clathrin-coated Vesicles, Sorting by Default in Endosomes, and Exocytosis via
913 RAB11-positive Carriers. MBoC *14*, 2029–2040.

914 Guglielmi, G., Barry, J.D., Huber, W., and De Renzis, S. (2015). An Optogenetic Method to
915 Modulate Cell Contractility during Tissue Morphogenesis. Developmental Cell *35*, 646–660.

916 Guo, H., Swan, M., Huang, S., and He, B. (2021). Mechanical bistability enabled by ectodermal
917 compression facilitates Drosophila mesoderm invagination.

918 He, B., Doubrovinski, K., Polyakov, O., and Wieschaus, E. (2014). Apical constriction drives
919 tissue-scale hydrodynamic flow to mediate cell elongation. Nature *508*, 392.

920 Heer, N.C., Miller, P.W., Chanet, S., Stoop, N., Dunkel, J., and Martin, A.C. (2017).
921 Actomyosin-based tissue folding requires a multicellular myosin gradient. Development *144*,
922 1876–1886.

923 Horgan, C.P., Hanscom, S.R., Jolly, R.S., Futter, C.E., and McCaffrey, M.W. (2010). Rab11-
924 FIP3 links the Rab11 GTPase and cytoplasmic dynein to mediate transport to the endosomal-
925 recycling compartment. Journal of Cell Science *123*, 181–191.

926 Jedd, G., Mulholland, J., and Segev, N. (1997). Two New Ypt GTPases Are Required for Exit
927 From the Yeast trans-Golgi Compartment. J Cell Biol *137*, 563–580.

928 Jewett, C.E., Vanderleest, T.E., Miao, H., Xie, Y., Madhu, R., Loerke, D., and Blankenship, J.T.
929 (2017). Planar polarized Rab35 functions as an oscillatory ratchet during cell intercalation in
930 the Drosophila epithelium. Nature Communications *8*, 476.

931 Jha, A., van Zanten, T.S., Philippe, J.-M., Mayor, S., and Lecuit, T. (2018). Quantitative Control
932 of GPCR Organization and Signaling by Endocytosis in Epithelial Morphogenesis. Current
933 Biology *28*, 1570-1584.e6.

934 Jodoin, J.N., Coravos, J.S., Chanet, S., Vasquez, C.G., Tworoger, M., Kingston, E.R., Perkins,
935 L.A., Perrimon, N., and Martin, A.C. (2015). Stable Force Balance between Epithelial Cells
936 Arises from F-Actin Turnover. Developmental Cell *35*, 685–697.

937 Karpova, N., Bobinnec, Y., Fouix, S., Huitorel, P., and Debec, A. (2006). Jupiter, a new
938 Drosophila protein associated with microtubules. Cell Motility *63*, 301–312.

939 Kennedy, M.J., Hughes, R.M., Peteya, L.A., Schwartz, J.W., Ehlers, M.D., and Tucker, C.L.
940 (2010). Rapid blue-light–mediated induction of protein interactions in living cells. Nature
941 Methods *7*, 973–975.

942 Kerridge, S., Munjal, A., Philippe, J.-M., Jha, A., de las Bayonas, A.G., Saurin, A.J., and Lecuit,
943 T. (2016). Modular activation of Rho1 by GPCR signalling imparts polarized myosin II
944 activation during morphogenesis. Nature Cell Biology *18*, 261–270.

945 Khandelwal, P., Prakasam, H.S., Clayton, D.R., Ruiz, W.G., Gallo, L.I., van Roekel, D.,
946 Lukianov, S., Peränen, J., Goldenring, J.R., and Apodaca, G. (2013). A Rab11a-Rab8a-Myo5B

network promotes stretch-regulated exocytosis in bladder umbrella cells. MBoC *24*, 1007–1019.

Kimura, K., Ito, M., Amano, M., Chihara, K., Fukata, Y., Nakafuku, M., Yamamori, B., Feng, J., Nakano, T., Okawa, K., et al. (1996). Regulation of Myosin Phosphatase by Rho and Rho-Associated Kinase (Rho-Kinase). Science *273*, 245–248.

Kirby, T.J., and Lammerding, J. (2016). Stretch to express. Nature Materials *15*, 1227–1229.

Ko, C.S., Tserunyan, V., and Martin, A.C. (2019). Microtubules promote intercellular contractile force transmission during tissue folding. J Cell Biol *218*, 2726–2742.

Langevin, J., Morgan, M.J., Rossé, C., Racine, V., Sibarita, J.-B., Aresta, S., Murthy, M., Schwarz, T., Camonis, J., and Bellaïche, Y. (2005). Drosophila Exocyst Components Sec5, Sec6, and Sec15 Regulate DE-Cadherin Trafficking from Recycling Endosomes to the Plasma Membrane. Developmental Cell *9*, 365–376.

Lapierre, L.A., Kumar, R., Hales, C.M., Navarre, J., Bhartur, S.G., Burnette, J.O., Provance, D.W., Mercer, J.A., Bähler, M., and Goldenring, J.R. (2001). Myosin Vb Is Associated with Plasma Membrane Recycling Systems. MBoC *12*, 1843–1857.

Le, T.P., and Chung, S. (2021). Regulation of apical constriction via microtubule- and Rab11-dependent apical transport during tissue invagination. BioRxiv 827378.

Le Droguen, P.-M., Claret, S., Guichet, A., and Brodu, V. (2015). Microtubule-dependent apical restriction of recycling endosomes sustains adherens junctions during morphogenesis of the Drosophila tracheal system. Development *142*, 363–374.

Lee, J.-Y., and Harland, R.M. (2010). Endocytosis Is Required for Efficient Apical Constriction during Xenopus Gastrulation. Current Biology *20*, 253–258.

Leptin, M., and Grunewald, B. (1990). Cell shape changes during gastrulation in Drosophila. Development *110*, 73–84.

Ligoxygakis, P., Roth, S., and Reichhart, J.-M. (2003). A Serpin Regulates Dorsal-Ventral Axis Formation in the Drosophila Embryo. Current Biology *13*, 2097–2102.

Lim, B., Levine, M., and Yamazaki, Y. (2017). Transcriptional Pre-patterning of Drosophila Gastrulation. Current Biology *27*, 286–290.

Lipatova, Z., Tokarev, A.A., Jin, Y., Mulholland, J., Weisman, L.S., and Segev, N. (2008). Direct Interaction between a Myosin V Motor and the Rab GTPases Ypt31/32 Is Required for Polarized Secretion. MBoC *19*, 4177–4187.

Lock, J.G., and Stow, J.L. (2005). Rab11 in Recycling Endosomes Regulates the Sorting and

979 Basolateral Transport of E-Cadherin. MBoC *16*, 1744–1755.

980 Manning, A.J., Peters, K.A., Peifer, M., and Rogers, S.L. (2013). Regulation of Epithelial
981 Morphogenesis by the G Protein–Coupled Receptor Mist and Its Ligand Fog. Sci. Signal. *6*,
982 ra98–ra98.

983 Martin, A.C. (2020). The Physical Mechanisms of Drosophila Gastrulation: Mesoderm and
984 Endoderm Invagination. Genetics *214*, 543–560.

985 Martin, A.C., and Goldstein, B. (2014). Apical constriction: themes and variations on a cellular
986 mechanism driving morphogenesis. Development *141*, 1987–1998.

987 Martin, A.C., Gelbart, M., Fernandez-Gonzalez, R., Kaschube, M., and Wieschaus, E.F. (2010).
988 Integration of contractile forces during tissue invagination. The Journal of Cell Biology *188*,
989 735–749.

990 Martin AC, Kaschube M, Wieschaus EF. Pulsed contractions of an actin-myosin network drive
991 apical constriction. Nature 2009;457:495–9.

992 Mason, F.M., Tworoger, M., and Martin, A.C. (2013). Apical domain polarization localizes
993 actin–myosin activity to drive ratchet-like apical constriction. Nat Cell Biol *15*, 926–936.

994 Mateus, A.M., Gorfinkiel, N., Schamberg, S., and Martinez Arias, A. (2011). Endocytic and
995 Recycling Endosomes Modulate Cell Shape Changes and Tissue Behaviour during
996 Morphogenesis in Drosophila. PLoS One *6*.

997 Mazumdar, A., and Mazumdar, M. (2002). How one becomes many: Blastoderm cellularization
998 in Drosophila melanogaster. BioEssays *24*, 1012–1022.

999 Miao, H., Vanderleest, T.E., Jewett, C.E., Loerke, D., and Blankenship, J.T. (2019). Cell
1000 ratcheting through the Sbf RabGEF directs force balancing and stepped apical constriction. J
1001 Cell Biol *218*, 3845–3860.

1002 Morize, P., Christiansen, A.E., Costa, M., Parks, S., and Wieschaus, E. (1998). Hyperactivation
1003 of the folded gastrulation pathway induces specific cell shape changes. Development *125*, 589–
1004 597.

1005 Moughamian, A.J., Osborn, G.E., Lazarus, J.E., Maday, S., and Holzbaur, E.L.F. (2013).
1006 Ordered Recruitment of Dynactin to the Microtubule Plus-End is Required for Efficient
1007 Initiation of Retrograde Axonal Transport. Journal of Neuroscience *33*, 13190–13203.

1008 Narumiya, S., Ishizaki, T., and Ufhata, M. (2000). Use and properties of ROCK-specific
1009 inhibitor Y-27632. In Methods in Enzymology, W.E. Balch, C.J. Der, and A. Hall, eds.
1010 (Academic Press), pp. 273–284.

1011 Nikolaidou, K.K., and Barrett, K. (2004). A Rho GTPase Signaling Pathway Is Used
1012 Reiteratively in Epithelial Folding and Potentially Selects the Outcome of Rho Activation.
1013 Current Biology *14*, 1822–1826.

1014 Ollion, J., Cochennec, J., Loll, F., Escudé, C., and Boudier, T. (2013). TANGO: a generic tool
1015 for high-throughput 3D image analysis for studying nuclear organization. Bioinformatics *29*,
1016 1840–1841.

1017 Ossipova, O., Kim, K., Lake, B.B., Itoh, K., Ioannou, A., and Sokol, S.Y. (2014). Role of Rab11
1018 in planar cell polarity and apical constriction during vertebrate neural tube closure. Nature
1019 Communications *5*, 3734.

1020 Ossipova, O., Chuykin, I., Chu, C.-W., and Sokol, S.Y. (2015). Vangl2 cooperates with Rab11
1021 and Myosin V to regulate apical constriction during vertebrate gastrulation. Development *142*,
1022 99–107.

1023 Otani, T., Oshima, K., Onishi, S., Takeda, M., Shinmyozu, K., Yonemura, S., and Hayashi, S.
1024 (2011). IKKε regulates cell elongation through recycling endosome shuttling. Dev Cell *20*,
1025 219–232.

1026 Pelissier, A., Chauvin, J.-P., and Lecuit, T. (2003). Trafficking through Rab11 Endosomes Is
1027 Required for Cellularization during Drosophila Embryogenesis. Current Biology *13*, 1848–
1028 1857.

1029 Pouille, P.-A., Ahmadi, P., Brunet, A.-C., and Farge, E. (2009). Mechanical Signals Trigger
1030 Myosin II Redistribution and Mesoderm Invagination in Drosophila Embryos. Sci. Signal. *2*,
1031 ra16–ra16.

1032 Razzell, W., Bustillo, M.E., and Zallen, J.A. (2018). The force-sensitive protein Ajuba regulates
1033 cell adhesion during epithelial morphogenesis. J Cell Biol *217*, 3715–3730.

1034 Riggs, B., Rothwell, W., Mische, S., Hickson, G.R.X., Matheson, J., Hays, T.S., Gould, G.W.,
1035 and Sullivan, W. (2003). Actin cytoskeleton remodeling during early Drosophila furrow
1036 formation requires recycling endosomal components Nuclear-fallout and Rab11. Journal of
1037 Cell Biology *163*, 143–154.

1038 Sawyer, J.K., Harris, N.J., Slep, K.C., Gaul, U., and Peifer, M. (2009). The Drosophila afadin
1039 homologue Canoe regulates linkage of the actin cytoskeleton to adherens junctions during
1040 apical constriction. Journal of Cell Biology *186*, 57–73.

1041 Schonteich, E., Wilson, G.M., Burden, J., Hopkins, C.R., Anderson, K., Goldenring, J.R., and
1042 Prekeris, R. (2008). The Rip11/Rab11-FIP5 and kinesin II complex regulates endocytic protein
1043 recycling. Journal of Cell Science *121*, 3824–3833.

1044 Schuh, M. (2011). An actin-dependent mechanism for long-range vesicle transport. Nature Cell

Biology *13*, 1431–1436.

Shillcock, J.C., and Lipowsky, R. (2005). Tension-induced fusion of bilayer membranes and vesicles. Nature Materials *4*, 225–228.

Siechen, S., Yang, S., Chiba, A., and Saif, T. (2009). Mechanical tension contributes to clustering of neurotransmitter vesicles at presynaptic terminals. Proceedings of the National Academy of Sciences *106*, 12611–12616.

Staykova, M., Holmes, D.P., Read, C., and Stone, H.A. (2011). Mechanics of surface area regulation in cells examined with confined lipid membranes. PNAS *108*, 9084–9088.

Sun, S., and Irvine, K.D. (2016). Cellular Organization and Cytoskeletal Regulation of the Hippo Signaling Network. Trends in Cell Biology *26*, 694–704.

Sweeton, D., Parks, S., Costa, M., and Wieschaus, E. (1991). Gastrulation in Drosophila: the formation of the ventral furrow and posterior midgut invaginations. Development *112*, 775–789.

Takahashi, S., Kubo, K., Waguri, S., Yabashi, A., Shin, H.-W., Katoh, Y., and Nakayama, K. (2012). Rab11 regulates exocytosis of recycling vesicles at the plasma membrane. J Cell Sci *125*, 4049–4057.

Tiwari, A.K., and Roy, J.K. (2008). Rab11 is essential for fertility in Drosophila. Cell Biology International *32*, 1158–1168.

Uhler, C., and Shivashankar, G.V. (2017). Regulation of genome organization and gene expression by nuclear mechanotransduction. Nature Reviews Molecular Cell Biology *18*, 717–727.

Ullrich, O., Reinsch, S., Urbé, S., Zerial, M., and Parton, R.G. (1996). Rab11 regulates recycling through the pericentriolar recycling endosome. J Cell Biol *135*, 913–924.

Vasquez, C.G., Tworoger, M., and Martin, A.C. (2014). Dynamic myosin phosphorylation regulates contractile pulses and tissue integrity during epithelial morphogenesis. J Cell Biol *206*, 435–450.

Vaughan, P.S., Miura, P., Henderson, M., Byrne, B., and Vaughan, K.T. (2002). A role for regulated binding of p150 *Glued* to microtubule plus ends in organelle transport. The Journal of Cell Biology *158*, 305–319.

Wang, Y., Huynh, W., Skokan, T.D., Lu, W., Weiss, A., and Vale, R.D. (2019). CRACR2a is a calcium-activated dynein adaptor protein that regulates endocytic traffic. The Journal of Cell Biology jcb.201806097.

1077 Wang, Y.-C., Khan, Z., Kaschube, M., and Wieschaus, E.F. (2012). Differential positioning of
1078 adherens junctions is associated with initiation of epithelial folding. Nature *484*, 390–393.

1079 Wang, Z., Edwards, J.G., Riley, N., Provance, D.W., Karcher, R., Li, X., Davison, I.G., Ikebe,
1080 M., Mercer, J.A., Kauer, J.A., et al. (2008). Myosin Vb Mobilizes Recycling Endosomes and
1081 AMPA Receptors for Postsynaptic Plasticity. Cell *135*, 535–548.

1082 Welz, T., Wellbourne-Wood, J., and Kerkhoff, E. (2014). Orchestration of cell surface proteins
1083 by Rab11. Trends in Cell Biology *24*, 407–415.

1084 Weng, M., and Wieschaus, E. (2016). Myosin-dependent remodeling of adherens junctions
1085 protects junctions from Snail-dependent disassembly. Journal of Cell Biology *212*, 219–229.

1086 Winter, C.G., Wang, B., Ballew, A., Royou, A., Karess, R., Axelrod, J.D., and Luo, L. (2001).
1087 Drosophila Rho-Associated Kinase (Drok) Links Frizzled-Mediated Planar Cell Polarity
1088 Signaling to the Actin Cytoskeleton. Cell *105*, 81–91.

1089 Woichansky, I., Beretta, C.A., Berns, N., and Riechmann, V. (2016). Three mechanisms control
1090 E-cadherin localization to the zonula adherens. Nature Communications *7*.

1091 Wu, X.-S., Elias, S., Liu, H., Heureaux, J., Wen, P.J., Liu, A.P., Kozlov, M.M., and Wu, L.-G.
1092 (2017). Membrane Tension Inhibits Rapid and Slow Endocytosis in Secretory Cells.
1093 Biophysical Journal *113*, 2406–2414.

1094 Yashiro, H., Loza, A.J., Skeath, J.B., and Longmore, G.D. (2014). Rho1 regulates adherens
1095 junction remodeling by promoting recycling endosome formation through activation of myosin
1096 II. MBoC *25*, 2956–2969.

1097 Yi, J.Y., Ori-McKenney, K.M., McKenney, R.J., Vershinin, M., Gross, S.P., and Vallee, R.B.
1098 (2011). High-resolution imaging reveals indirect coordination of opposite motors and a role for
1099 LIS1 in high-load axonal transport. Journal of Cell Biology *195*, 193–201.

1100

1101 ***Figures and Figure Legends:***

1102 **Figure 1**

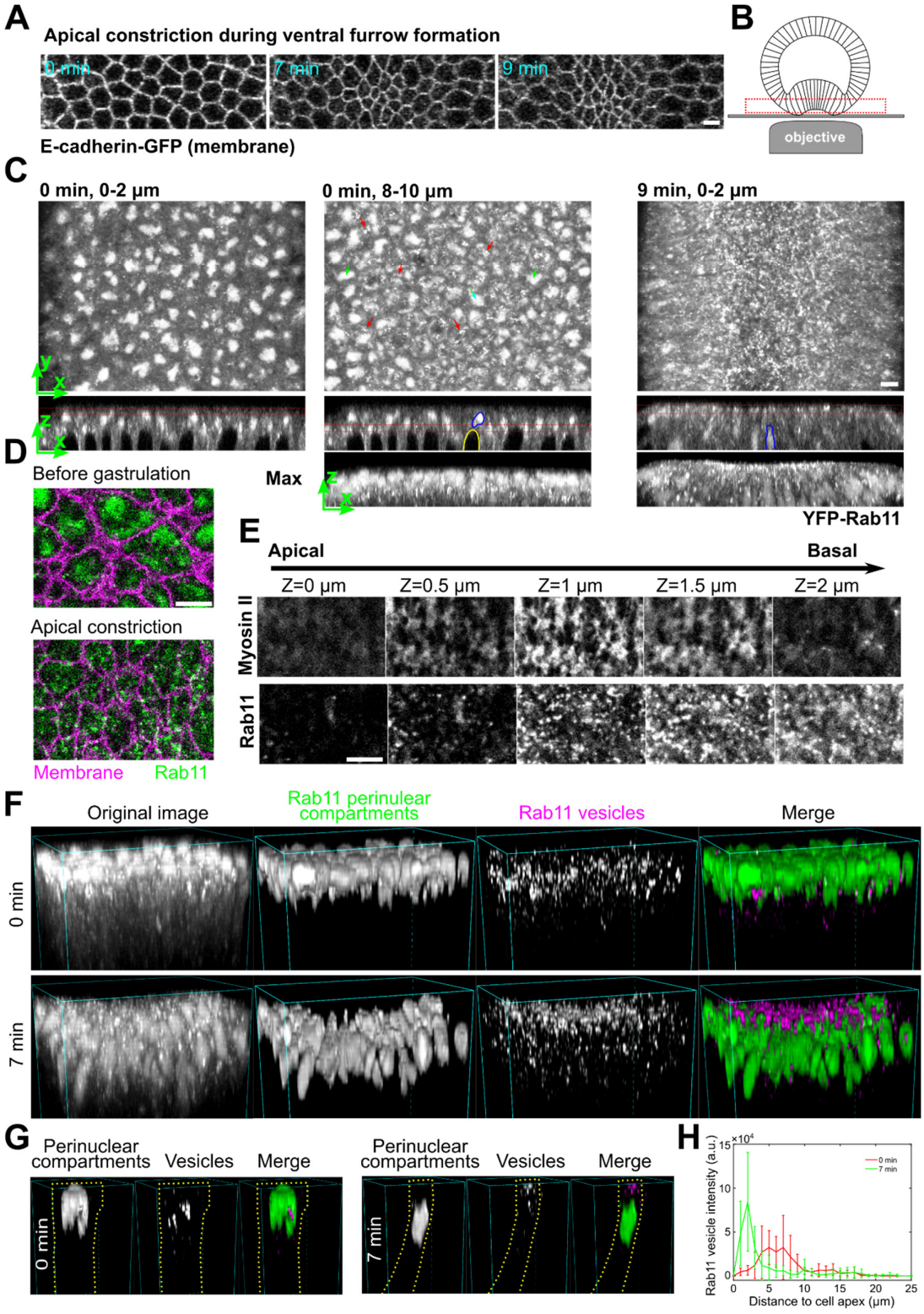

1103

1104 **Figure 1. Rab11-positive vesicle-like structures accumulate apically in constricting cells**

1105 **during ventral furrow formation**

1106 **(A)** Apical constriction during ventral furrow formation. Scale bar, 10 μm.

1107 **(B)** The imaging setup for acquiring the en face view of constricting cells.

1108 **(C)** Rab11 compartments (endogenous YFP-Rab11) in an embryo at the onset (0 min) and 9

1109 min into ventral furrow formation. Top panel, maximum projection over 2 μm depth from en

1110 face view; middle and bottom panels, a single slice and maximum projection of the cross-

1111 section view, respectively. Red boxes: Z position of the corresponding en face view. Red

1112 arrows: perinuclear Rab11 vesicles; green arrows and blue outlines: perinuclear Rab11

1113 compartments; yellow outline: nucleus.

1114 **(D)** Zoom-in view of a small ROI in the ventral region of the embryo.

1115 **(E)** Montage showing Rab11 and Myosin II distribution over depth during apical

1116 constriction.

1117 **(F, G)** 3D reconstruction of Rab11 positive structures in ventral mesoderm constricting cells.

1118 0 min: onset of gastrulation. Rab11 perinuclear compartments and vesicles are segmented

1119 separately using ilastik. An individual cell is shown in G as an example. Cell outlines (yellow

1120 dotted lines) are determined based on Gap43-mCherry signal.

1121 **(H)** The intensity profile of summed intensity of Rab11 vesicles along Z direction. 0 μm: cell

1122 apex. Error bar: s.d. N = 13 cells.

1123 All scale bars are 5 μm unless mentioned otherwise.

1124 **Figure 2**

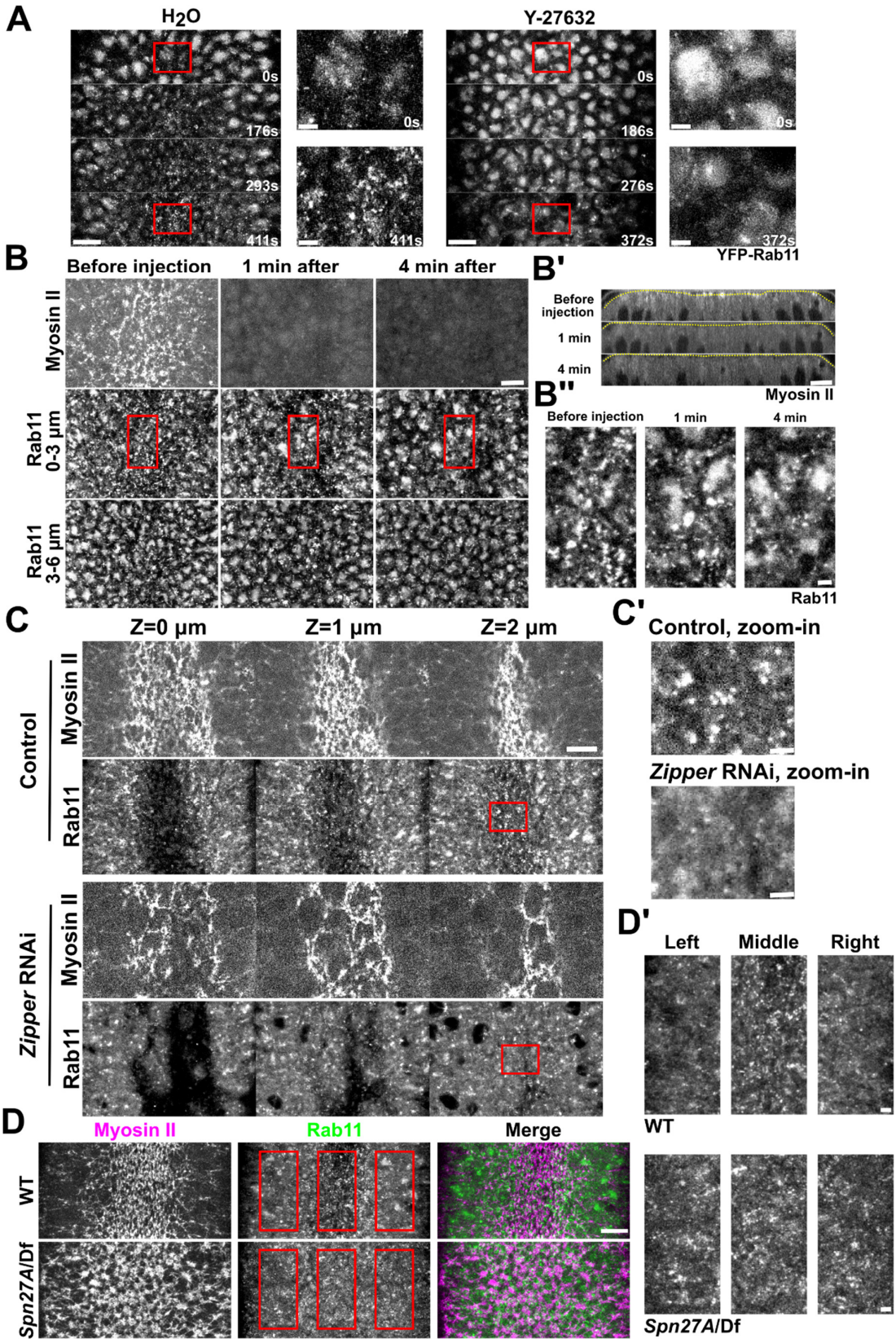

1125

1126 **Figure 2. Apical accumulation of Rab11 vesicles depends on apical Myosin II activation**

1127 **(A)** Inhibition of Myosin II activation by Y-27632 injection at late cellularization prevents

1128 apical Rab11 vesicle accumulation. (A') Zoom-in view of the outlined region in A. 0 sec:

1129 onset of gastrulation. Y-27632 injection: N = 4 embryos; H_2O injection: N = 3 embryos.

1130 **(B)** Injection of Y-27632 during apical constriction causes rapid diminishing of apical Rab11

1131 vesicles. N = 4 embryos. (B') Cross-section view. Yellow lines: apical surface. (B'') Zoom-in

1132 view of B.

1133 **(C)** Knockdown of myosin heavy chain Zipper inhibits apical accumulation of Rab11 vesicle.

1134 N = 4 embryos for each genotype. (C') Zoom-in view of C.

1135 **(D)** *Spn27A*/Df mutant embryos exhibit ventralized phenotype with expanded domain of

1136 apical Myosin II activation and apical Rab11 vesicle accumulation (N = 3 embryos). (D')

1137 Zoom-in view of D. Images were Gaussian filtered with a radius of 0.5 pixel. Fewer z-slices

1138 were projected for the zoom-in view to improve the signal/noise.

1139 All scale bars for zoom-in view, 2 μm; scale bars for the rest, 10 μm. All en face views are

1140 maximum projections of a ~3 – 4 μm-stack below apical surface of the constriction domain.

1141

1142 **Figure 3**

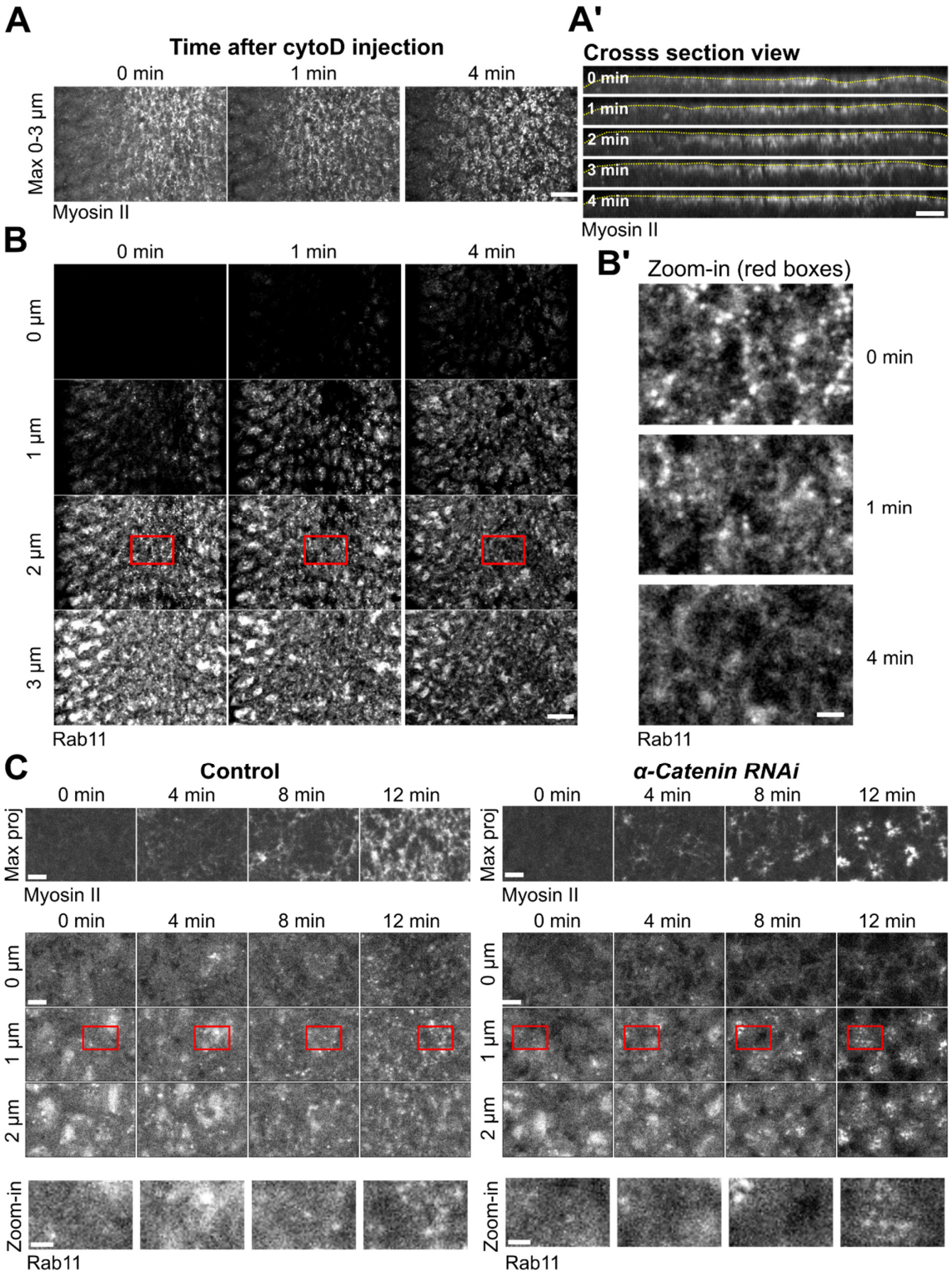

1143

1144 **Figure 3. Apical accumulation of Rab11 vesicles depends on F-actin but not does not**

1145 **require intact AJs**

1146 **(A, A', B, B')** Cytochalasin D injection (0 min) during apical constriction results in rapid

1147 diminishing of apical Rab11 vesicles without causing immediate apical myosin loss. (A)

1148 Maximum projection of apical Myosin II. Scale bar, 10 µm. (A') Cross-section view. Yellow

1149 lines: apical surface. Scale bar, 10 µm. (B) Enface view showing apical Rab11 vesicles. Scale

1150 bar, 10 µm. (B') Zoom-in view of B. Scale bar, 2 µm.

1151 **(C)** Knockdown of junctional component α-Catenin does not prevent apical accumulation of

1152 Rab11 vesicles. Scale bars, 5 µm. Scale bars for zoom-in view, 2 µm.

1153 **Figure 4**

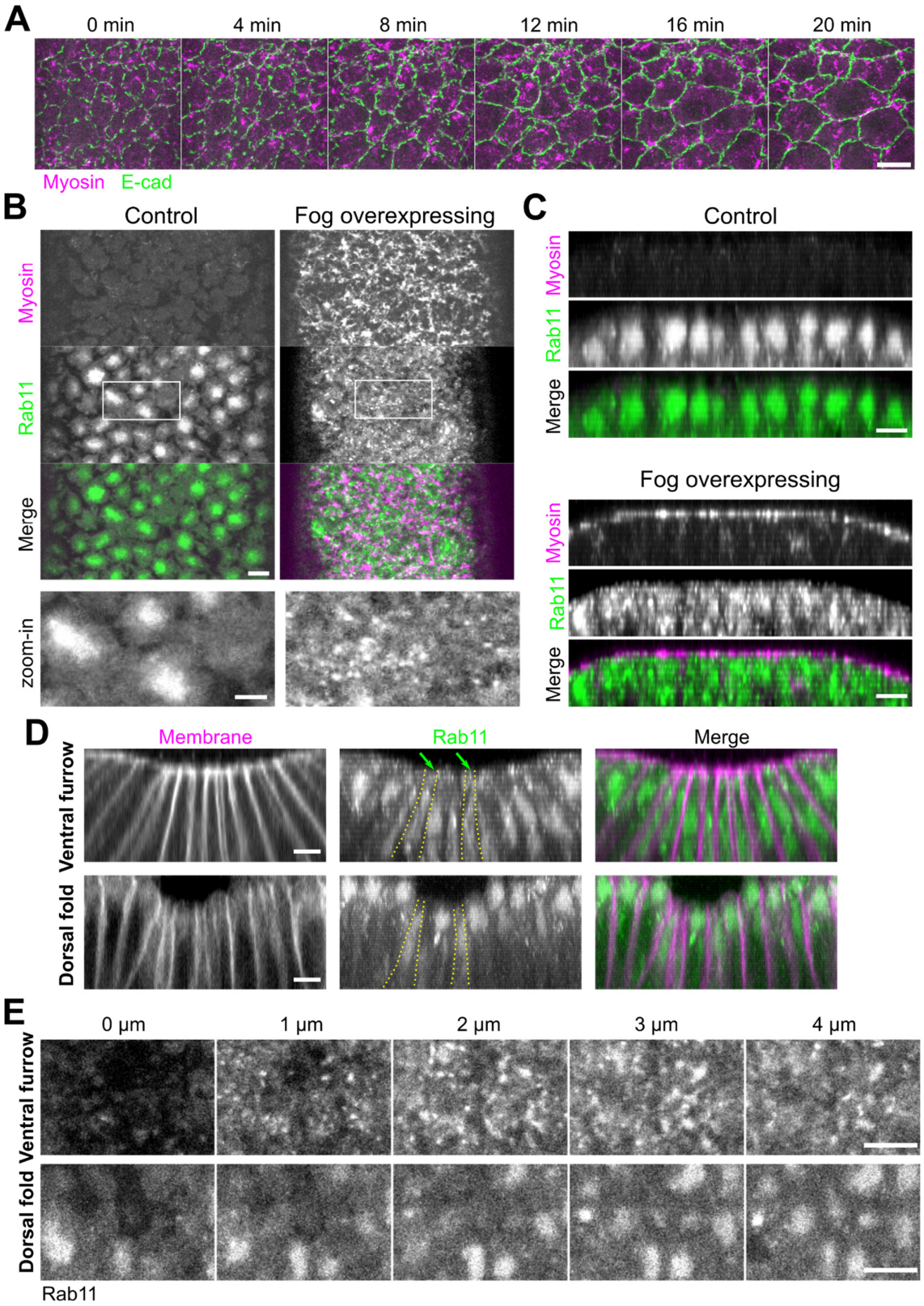

1154

1155 **Figure 4. Apical actomyosin activation, but not apical cell area reduction, is critical for**

1156 **apical accumulation of Rab11 vesicles**

1157 **(A)** Ectopic expression of Fog results in Myosin II activation in dorsal cells but does not

1158 cause apical area reduction. N = 3 embryos. Scale bar, 10 µm.

1159 **(B, C)** Ectopic activation of Myosin II in dorsal cells by overexpression of Fog induces

1160 ectopic apical accumulation of Rab11 vesicles. (B) Enface view. (C) Cross section view.

1161 Scale bars, 5 µm. Scale bar for zoom-in view, 2 µm.

1162 **(D, E)** Comparison of YFP-Rab11 in ventral furrow and dorsal fold. Yellow outlines:

1163 example cells displaying apical area reduction. Dorsal fold cells do not show apical Rab11

1164 vesicle accumulation despite undergoing apical shrinking. (D) and (E): Cross-section view

1165 and en face view, respectively. Scale bar, 5 µm. Green arrows: Rab11 vesicles. Scale bar, 5

1166 µm.

1167

1168 **Figure 5**

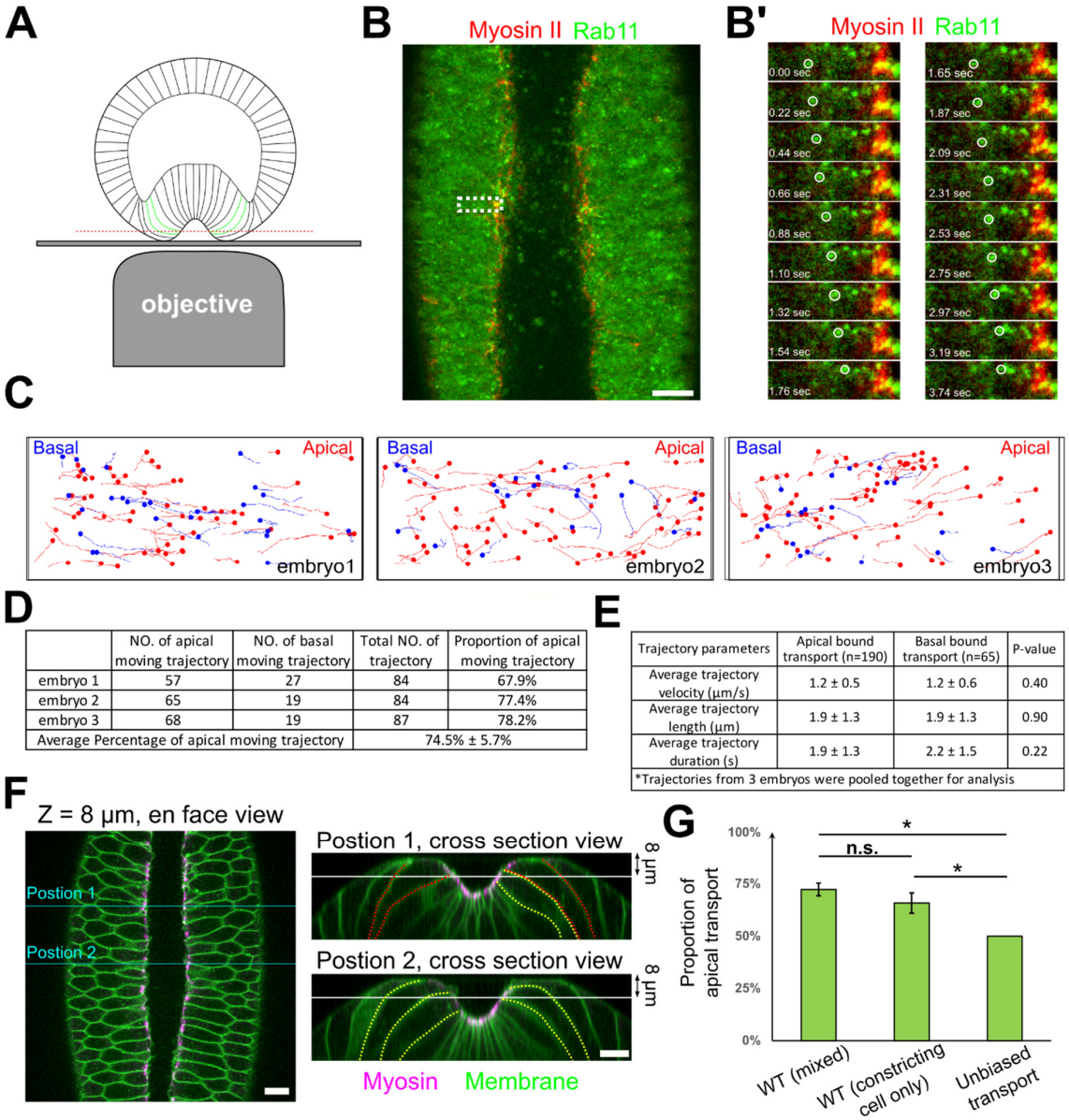

D

	NO. of apical moving trajectory	NO. of basal moving trajectory	Total NO. of trajectory	Proportion of apical moving trajectory
embryo 1	57	27	84	67.9%
embryo 2	65	19	84	77.4%
embryo 3	68	19	87	78.2%
Average Percentage of apical moving trajectory			74.5% ± 5.7%	

E

Trajectory parameters	Apical bound transport (n=190)	Basal bound transport (n=65)	P-value
Average trajectory velocity (μm/s)	1.2 ± 0.5	1.2 ± 0.6	0.40
Average trajectory length (μm)	1.9 ± 1.3	1.9 ± 1.3	0.90
Average trajectory duration (s)	1.9 ± 1.3	2.2 ± 1.5	0.22
*Trajectories from 3 embryos were pooled together for analysis			

1169

1170

1171 **Figure 5. Rab11 vesicles are transported apical-basally with a strong bias in the apical**

1172 **direction**

1173 **(A)** Imaging configuration to capture the movement of Rab11 vesicles along the apical-basal

1174 direction. Red line: imaging plane. Green outlines: constricting cells being imaged.

1175 **(B, B')** Surface view of an embryo imaged as depicted in A. Scale bar, 10 µm. (B'): zoom-in

1176 view of B showing the apical movement of two Rab11 vesicles (white circles). Scale bar, 2

1177 µm.

1178 **(C)** Vesicle trajectories in 3 wildtype embryos in a ~35-sec time window. Red and blue mark

1179 apical- and basal-bound trajectories, respectively.

1180 **(D)** Counts of apically and basally oriented trajectories.

1181 **(E)** Comparison of average trajectory length, velocity and duration (mean ± s.d.) shows no

1182 significant difference between apically and basally directed transport. Two tailed Student's t-

1183 test; N = 3 embryos.

1184 **(F)** Left: Enface view of an embryo expressing both myosin and membrane markers. Right:

1185 Cross-section view of the same embryo at the indicated A-P positions (cyan lines). White

1186 line: imaging plane; yellow and red outlines: cells with or without obvious apical shrinking,

1187 respectively. Scale bars, 10 µm.

1188 **(G)** Rab11 vesicles exhibit directional bias towards the apical side. WT (cells with apical

1189 Myosin II activation): quantification of movies with Myosin II and Rab11 markers. The ROI

1190 may include a mixture of apically constricted and non-constricted cells that exhibited apical

1191 myosin accumulation. WT (constricting cell only): quantification of movies with membrane

1192 and Rab11 markers. Only apically constricted cells are quantified (Methods). Two tailed one-

1193 sample t-test against 50% was used for comparison to hypothetical unbiased transport. Two

1194 tailed Student's t test was used for comparison between two WT samples. N = 3 embryos for

1195 each category.

1196 For all panels, error bar: s.d.; ***: $p < 0.001$; **: $p < 0.01$; *: $p < 0.05$; n.s.: $p > 0.05$.

1197

1198 **Figure 6**

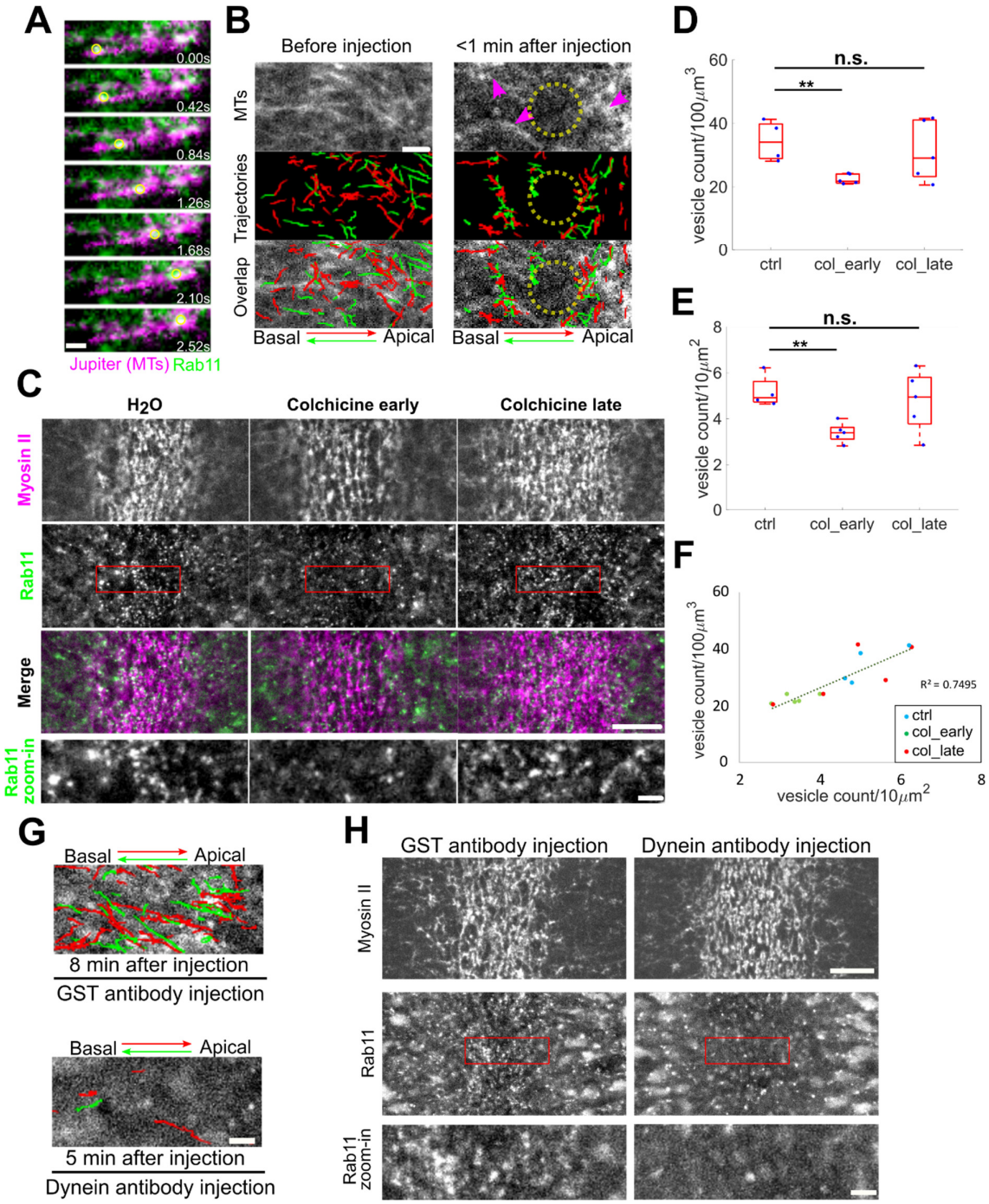

1199
1200

1201 **Figure 6. Rab11 vesicle transport requires microtubules and dynein**

1202 **(A)** An example of Rab11 vesicle movement (yellow circle) along the microtubules (Jupiter-
1203 GFP). Scale bar, 1 μm.

1204 **(B)** Acute disruption of microtubules via colchicine injection results in immediate inhibition
1205 of Rab11 vesicle transport. Magenta arrowheads: residual microtubules. Yellow circles:
1206 region where microtubules were completely disrupted. Scale bar, 2 μm.

1207 **(C)** En face view of the constricting domain shortly (< 2 min) after on-stage injection of
1208 water or colchicine. Injection of colchicine shortly before but not after the onset of
1209 gastrulation (N = 5 embryos for each condition) results in reduced Rab11 vesicle
1210 accumulation compared to water injected controls (N = 4 embryos). Scale bar, 10 μm. Bottom
1211 panels: zoom-in views. Scale bar, 2 μm.

1212 **(D-F)** Quantification of Rab11 vesicle density after water or colchicine injection within a 3.5
1213 μm-stack from apical surface (D) or in a single z plane near apical surface (E) generates
1214 consistent results (F).

1215 **(G)** Injection of dynein antibody rapidly abolishes both apical (red) and basal (green)
1216 transport of Rab11 vesicles. Trajectories show vesicle movement within a 20-sec window at
1217 the indicated time after injection. N = 5 embryos for each condition. Scale bar, 2 μm.

1218 **(H)** En face view showing inhibition of apical accumulation of Rab11 vesicles upon on-stage
1219 injection of dynein antibody immediately before the onset of gastrulation. N = 5 and 6
1220 embryos for GST antibody and dynein antibody injection, respectively. Scale bar, 10 μm.
1221 Bottom panels: zoom-in views. Scale bar, 2 μm.

Figure 7

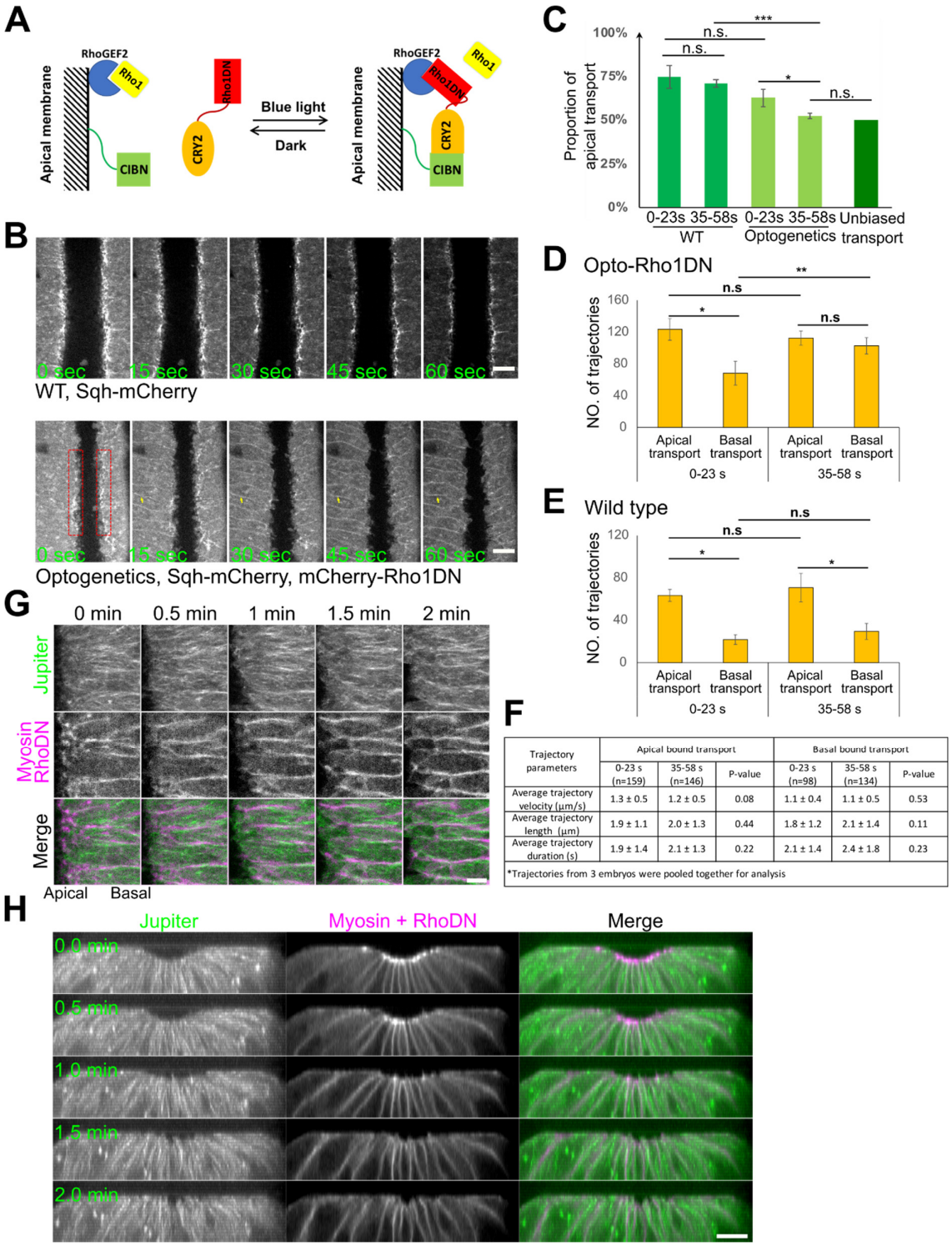

F

Trajectory parameters	Apical bound transport			Basal bound transport		
	0-23 s (n=159)	35-58 s (n=146)	P-value	0-23 s (n=98)	35-58 s (n=134)	P-value
Average trajectory velocity (μm/s)	1.3 ± 0.5	1.2 ± 0.5	0.08	1.1 ± 0.4	1.1 ± 0.5	0.53
Average trajectory length (μm)	1.9 ± 1.1	2.0 ± 1.3	0.44	1.8 ± 1.2	2.1 ± 1.4	0.11
Average trajectory duration (s)	1.9 ± 1.4	2.1 ± 1.3	0.22	2.1 ± 1.4	2.4 ± 1.8	0.23

*Trajectories from 3 embryos were pooled together for analysis

1225 **Figure 7. The apical bias of Rab11 vesicle transport depends on activation of apical**

1226 **actomyosin contractility**

1227 **(A)** Diagram depicting optogenetic inhibition of Myosin II activation by Opto-Rho1DN.

1228 **(B)** Top: upon continuous blue light stimulation, Rho1DN is immediately recruited to the

1229 plasma membrane (yellow arrows). Apical myosin II (red boxes) disappears ~ 30 sec after

1230 stimulation. Bottom: A control embryo at similar stage of furrow formation. Scale bar, 10 μm.

1231 **(C – F)** The apical bias of the transport is abolished in less than one minute after Opto-

1232 Rho1DN stimulation (C, n = 3 embryos). This change is caused by a significant increase in

1233 the number of basally directed transport events (D), which is not observed in wildtype

1234 embryos (E, n = 3 embryos). There is no significant difference on average trajectory velocity,

1235 length and duration of apical and basal bound transports between 0 – 23 sec and 35 – 58 sec

1236 post stimulation windows (F, mean ± s.d.). Two tailed one-sample t-test against 50% was

1237 used for comparison to hypothetical unbiased transport. Two tailed Student's t test was used

1238 for comparison between conditions.

1239 **(G, H)** Microtubules do not exhibit obvious changes in intensity or overall organization in the

1240 first two minutes after Opto-Rho1DN stimulation (0 min). (G) En face maximum intensity

1241 projection of the apical surface (5 μm thick) showing microtubules (GFP-Jupiter) in an embryo

1242 stimulated at the stage comparable to that in B. Scale bar, 5 μm. (H) Cross section view showing

1243 an embryo stimulated at a stage slightly earlier than that in (G). Scale bar, 10 μm.

1244

1245 **Figure 8**

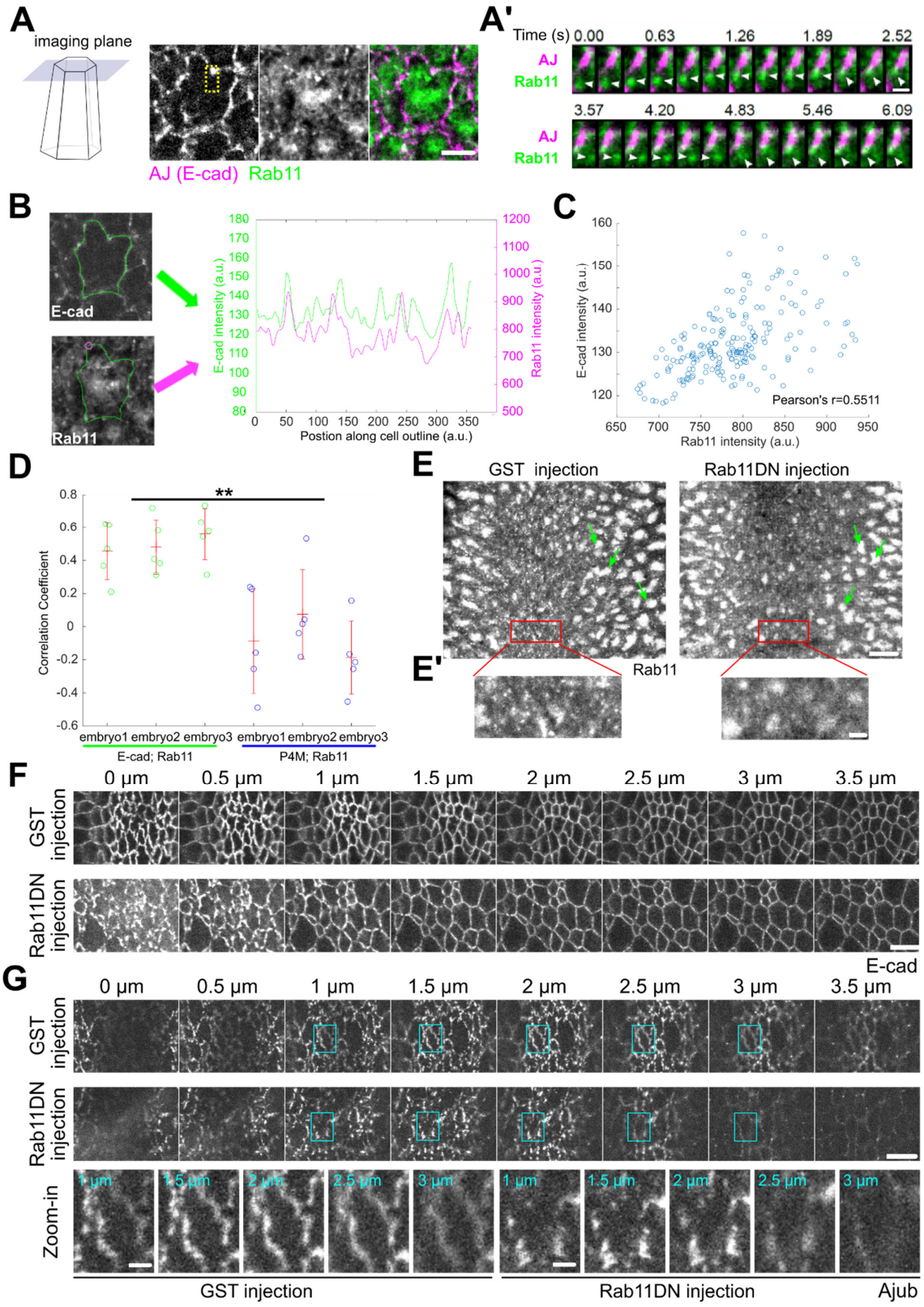

1246

1247 **Figure 8. Rab11 reinforces the apical AJs during ventral furrow formation**

1248 **(A)** Capturing apical Rab11 vesicle dynamics with single-plane fast imaging. Example of a
1249 single constricting cell is shown. Scale bar, 5 μm. (A') zoom-in view of (A) showing two
1250 Rab11 vesicles moving towards an adherens junction spot. Scale bar, 1 μm.

1251 **(B-D)** Analysis of spatial correlation between Rab11 vesicles and AJs. (B) The same
1252 constricting cell as shown in (A) is outlined in green. Magenta circle: an example sampling
1253 region within which Rab11 signal is measured. Right panel: the intensity profiles of E-
1254 cadherin and Rab11 along the indicated cell outline. (C) E-cadherin intensities for all points
1255 along the cell outline plotted against the corresponding Rab11 intensities. (D) Rab11 shows a
1256 significantly higher correlation with E-cadherin than with a general membrane marker P4M
1257 (N = 3 embryos for each genotype, 5 cells per embryo). Two tailed Student's t-test was used
1258 for statistical comparison.

1259 **(E)** Injection of Rab11DN rapidly eliminates apical Rab11 vesicles but does not immediately
1260 affect the perinuclear Rab11 compartments (green arrows). Scale bar, 10 μm. (E') Zoom-in
1261 view of (E). Scale bar, 2 μm.

1262 **(F)** Rab11DN injection affects the integrity of apical AJs in the constricting cells. 14 out of
1263 19 Rab11DN injected embryos show fragmented apical AJs while 8 of 8 GST injected
1264 embryos show relatively continuous AJs. Scale bar, 5 μm.

1265 **(G)** Ajub shows reduced enrichment at the apical AJs during apical constriction in Rab11DN
1266 injected embryos compared to the control embryos (N = 4 embryos for each condition). Scale
1267 bar, 5 μm. Bottom, enlarged view of one cell (cyan boxes) as an example. Scale bar, 1 μm.

1268 **Figure 9**

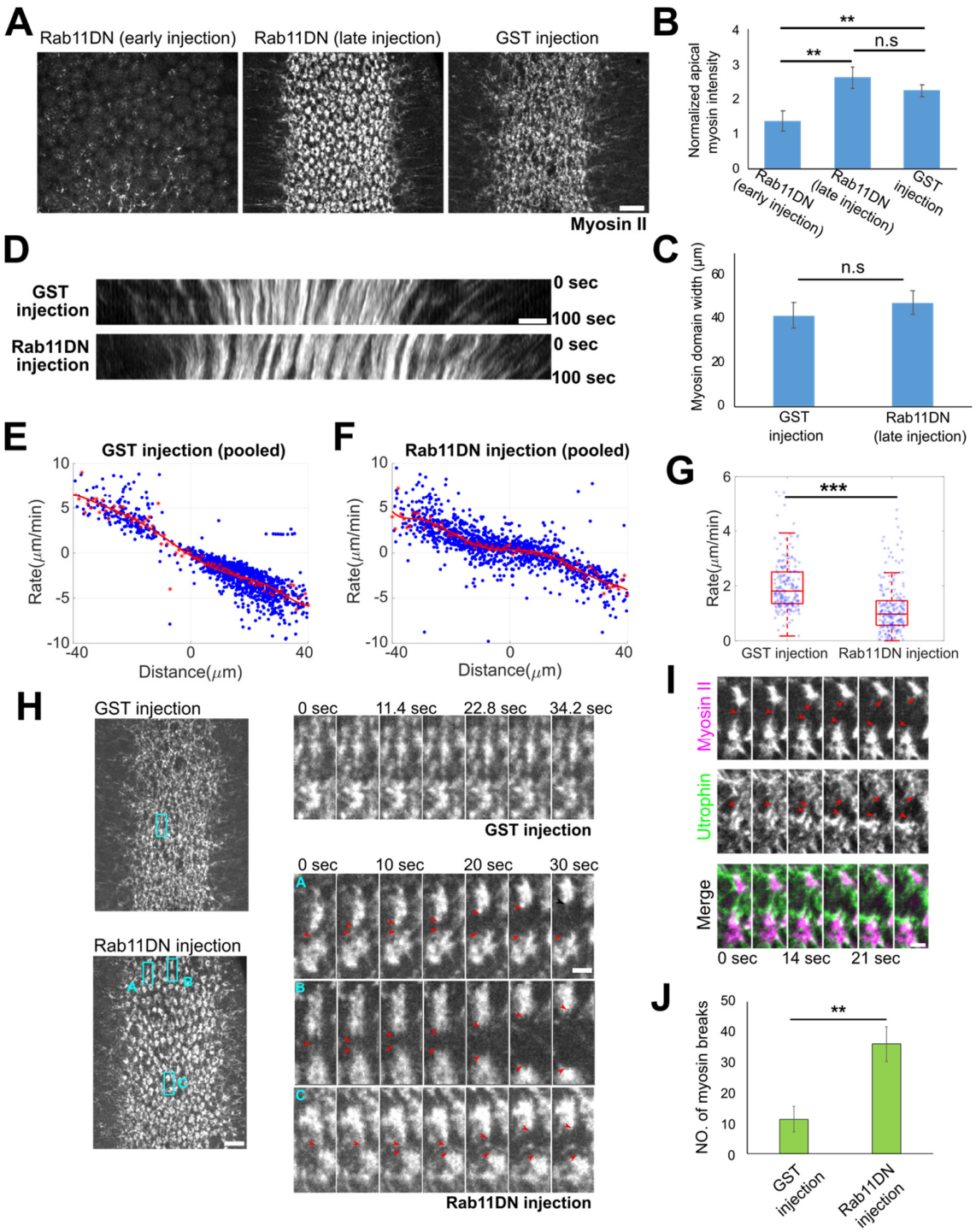

1269
1270

1271 **Figure 9. Acute inhibition of Rab11 results in defects in Myosin II organization and**

1272 **apical constriction**

1273 **(A-C)** Stage-dependent effect of Rab11DN injection on apical myosin network. (A): Injection

1274 of Rab11DN at early cellularization (> 30 min before onset of gastrulation) impairs apical

1275 myosin II activation (N = 3 embryos), whereas injection around the onset of gastrulation does

1276 not affect myosin II activation but causes defects in apical myosin organization (N = 4

1277 embryos). GST injection: N = 3 embryos. Scale bar, 10 μm. (B, C): Quantification of apical

1278 myosin II intensity (B) and the width of myosin domain (C) at ~6-7 min after the onset of

1279 gastrulation. Two tailed Student's t-test was used for statistical comparison.

1280 **(D)** Example kymograph showing the movement of apical myosin II towards ventral midline

1281 at ~6-7 minutes into gastrulation. Only the late Rab11DN injected embryos were analyzed in

1282 (D) – (K). Scale bar, 5 μm.

1283 **(E – G)** Quantification of apical constriction rate in embryos injected with GST and

1284 Rab11DN. (E, F) Rate of ventral movement of myosin structures as a function of their initial

1285 position relative to the ventral midline. Red asterisks: average velocity. Red curve:

1286 polynomial fit. (G) Rate for myosin structures located 10-15 μm away from the ventral

1287 midline. Two tailed Student's t test was used for statistical comparison.

1288 **(H – J)** Rab11DN injection increases the frequency of myosin breaks during apical

1289 constriction. (H) Left, representative surface views of the supracellular myosin network.

1290 Scale bar, 10 μm. Right, zoom-in view showing myosin dynamics over time. Red

1291 arrowheads: myosin breaks. Scale bar, 2 μm. (I) Myosin breaks are associated with breaks in

1292 the underlying F-actin network (UtrophinABD-Venus). Scale bar, 2 μm. N = 3 embryos for

1293 each condition. (J) Quantification of the number of myosin breaks over a ~100-sec time

1294 window at ~6 – 7 min after apical constriction starts. Two tailed Student's t test was used for

1295 statistical comparison.

1296

Figure 10

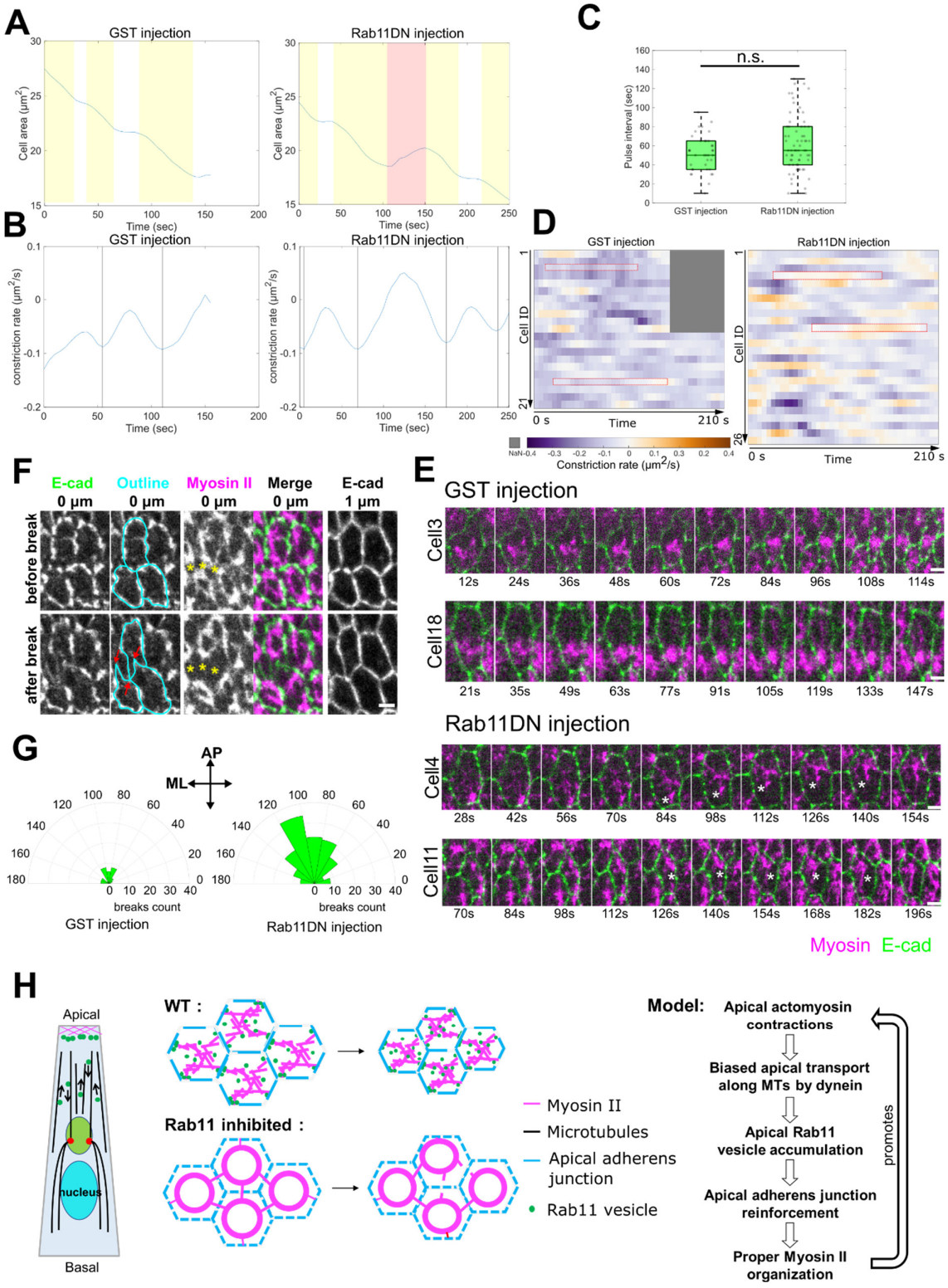
A
GST injection
Rab11DN injection
Cell area (μm²)
Time (sec)
B
constriction rate (μm²/s)
C
n.s.
Pulse interval (sec)
GST injection
Rab11DN injection
D
Cell ID
Time
0 s
210 s
Constriction rate (μm²/s)
E
GST injection
Cell3
Cell18
Rab11DN injection
Cell4
Cell11
Myosin E-cad
F
E-cad 0 μm
Outline 0 μm
Myosin II 0 μm
Merge 0 μm
E-cad 1 μm
before break
after break
G
AP
ML
breaks count
GST injection
Rab11DN injection
H
Apical
nucleus
Basal
WT :
Rab11 inhibited :
Myosin II
Microtubules
Apical adherens junction
Rab11 vesicle
Model:
Apical actomyosin contractions
Biased apical transport along MTs by dynein
Apical Rab11 vesicle accumulation
Apical adherens junction reinforcement
Proper Myosin II organization
promotes

1299 **Figure 10. Rab11DN injection results in increased frequency of apical re-expansion**

1300 **during apical constriction**

1301 **(A, B)** Example cell area change and constriction rate over time in GST and Rab11DN

1302 injected embryos. Yellow shaded area, constriction phase; white area, stabilization phase; red

1303 shaded area, apical re-expansion. Vertical lines in B: peak of constriction rate.

1304 **(C)** Rab11DN injection does not affect the frequency of cell constriction pulses. Pulse

1305 interval was calculated as the interval between neighboring constriction peaks.

1306 **(D, E)** Rab11DN injected embryos exhibited increased frequency of apical re-expansion

1307 events. (D) Heatmap showing constriction rate of individual cell over ~200 sec window

1308 during mid-apical constriction phase in GST and Rab11DN injected embryos. Positive

1309 constriction rate indicates apical re-expansion. N = 21 cells from 2 GST-injected embryos. N

1310 = 26 cells from 2 Rab11DN-injected embryos. Red boxes correspond to the examples shown

1311 in (E). Asterisks in (E): gaps resulted from myosin break event. Scale bars, 2 μm.

1312 (F) Apical AJ is pulled inward (red arrows) when myosin break (yellow asterisks) occurs in

1313 the adjacent cell. Scale bar, 2 μm.

1314 (G) Quantification of myosin break orientation in GST- and Rab11DN-injected embryos.

1315 Dataset from figure 9 (late injection) was used for this analysis.

1316 **(H)** Schematics of proposed actomyosin-dependent feedback mechanism.

1317 **Supplemental Figure 1**

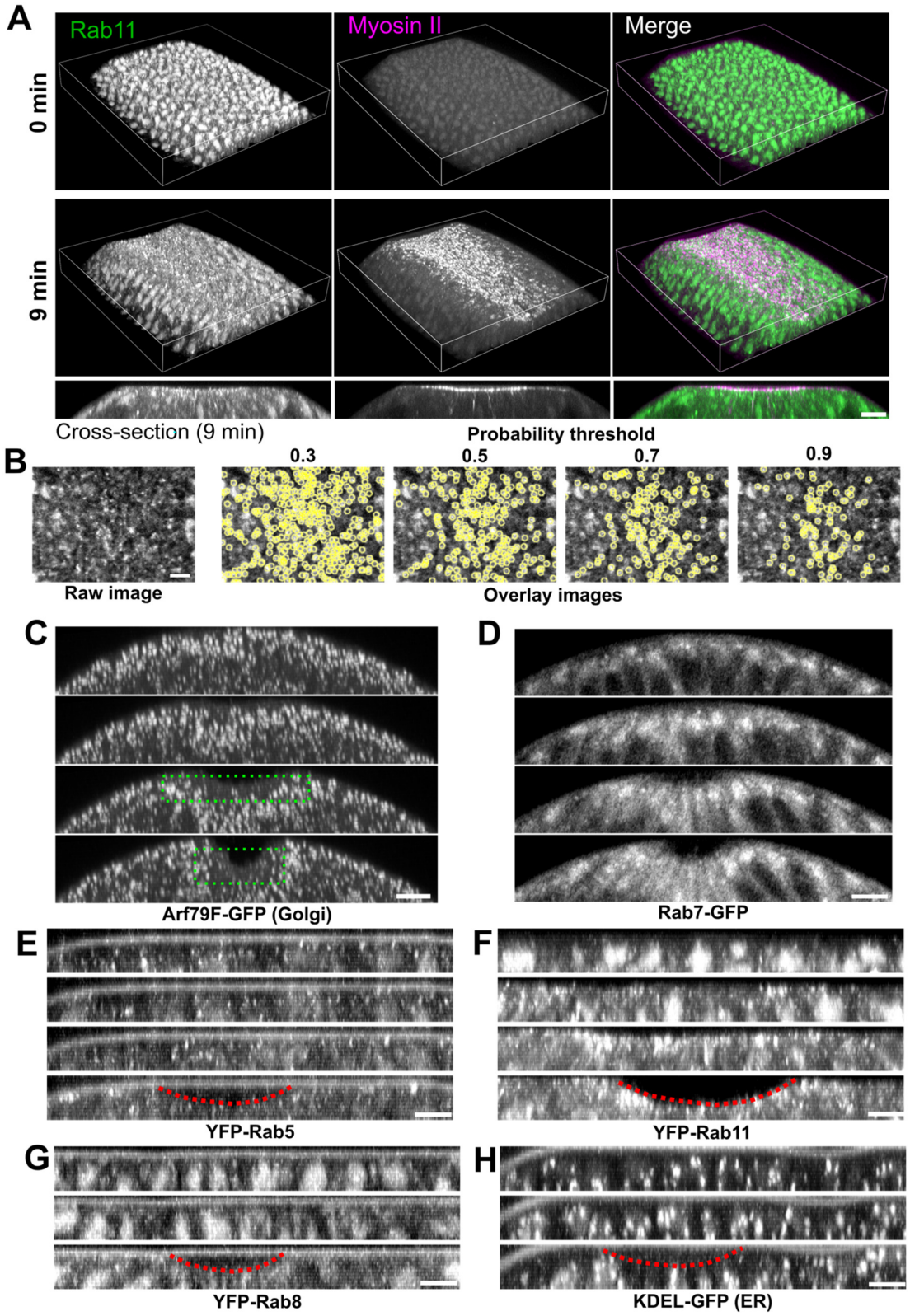

1318

1319 **Figure S1. Localization of Rab11 and other endomembrane compartments during**

1320 **ventral furrow formation**

1321 **(A)** 3D reconstruction of the ventral part of an embryo expressing YFP-Rab11 and mCherry-

1322 Sqh during ventral furrow formation showing apical accumulation of Rab11 vesicles in

1323 constricting cells. Magenta box indicates the apical region of the constricting cells. Bottom

1324 panel are the cross-section view images of the same embryo. Scale bar, 10 μm.

1325 **(B)** Vesicle segmentation using different probability threshold. Vesicles are segmented based

1326 on the probability map generated by ilastik. Threshold of 0.7 gives best quality of

1327 segmentation.

1328 **(C-H)** Localization change of different compartment markers in the ventral cross-section

1329 view of embryos. from late cellularization (top image in each panel) to early gastrulation.

1330 (C) Golgi marker Arf79F. Green dotted box shows the lack of Golgi puncta in the apical

1331 region of the constricting domain. (D) Late endosome marker Rab7. (E) Early endosome

1332 marker YFP-Rab5. (F) Recycling endosome marker YFP-Rab11. (G) YFP-Rab8. (H) ER

1333 marker KDEL-GFP. Among all the organelles examined here, Rab11 positive structures

1334 exhibit the most striking morphology and localization changes during ventral furrow

1335 formation. Images in A and B were taken on a multiphoton microscope. Scale bars, 10 μm.

1336 Images in C – F were taken on a spinning disk confocal microscope. Red dotted lines indicate

1337 the ventral furrow. Scale bars, 5 μm. The cross-section views were made by maximum

1338 intensity projection over 4 – 5 μm.

1339

Supplemental Figure 2

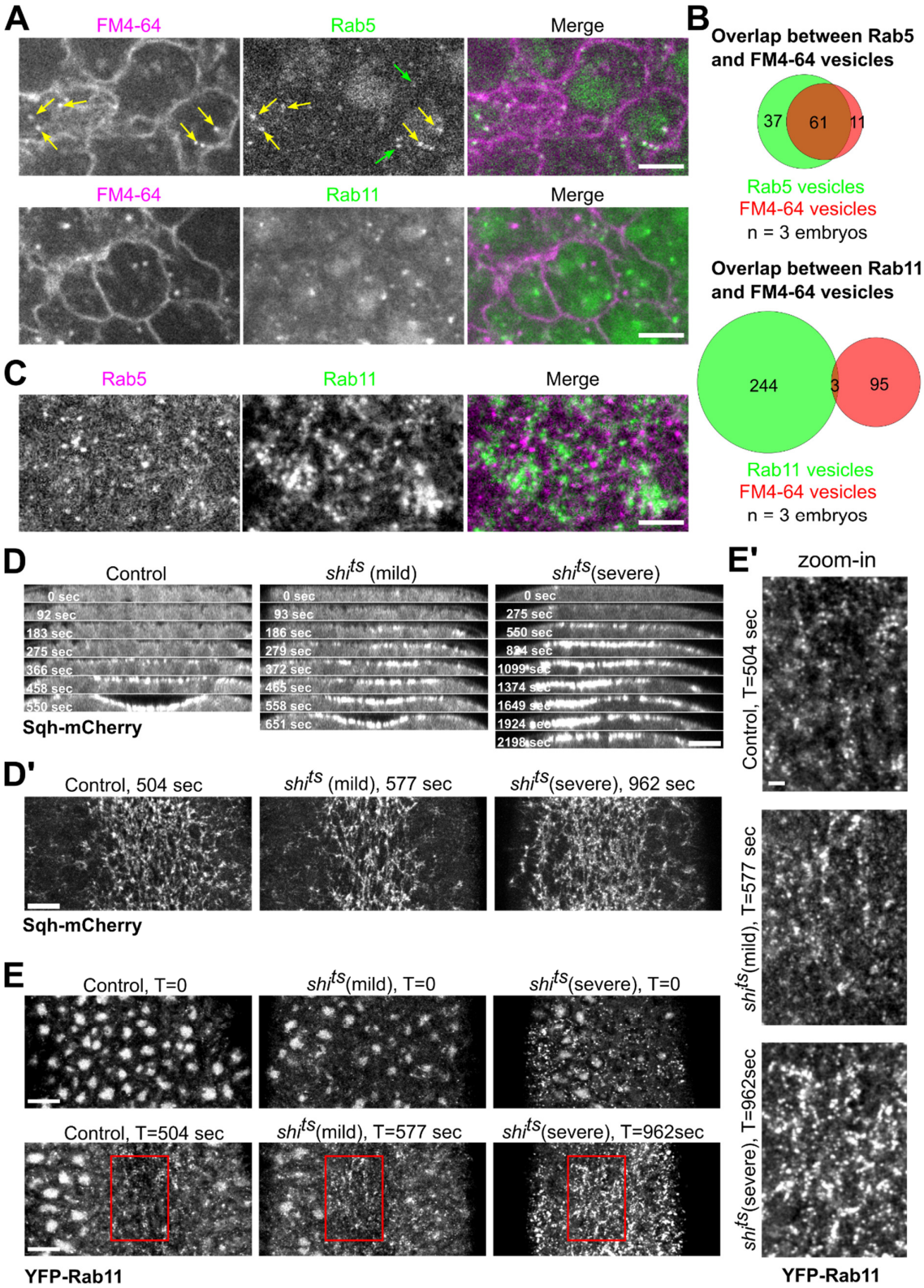

1343 **Figure S2. Apical Rab11 vesicles are not derived from endocytosis**

1344 **(A)** Endocytosed positive vesicles labeled by membrane dye FM4-64 extensively colocalize
1345 with YFP-Rab5 vesicles (85%, 72 vesicles from 3 embryos) but not YFP-Rab11 vesicles (3%,
1346 98 vesicles from 3 embryos) during apical constriction. Green arrows mark Rab5 vesicles
1347 that do not colocalize with FM4-64 vesicles and yellow arrows mark Rab5 vesicles that
1348 colocalize with FM4-64 vesicles. Scale bar, 5 μm.

1349 **(B)** Quantification of colocalization between endocytosed FM4-64 vesicles and
1350 corresponding Rab vesicles.

1351 **(C)** YFP-Rab5 and mCherry-Rab11 vesicles do not show colocalization. Scale bar, 5 μm.

1352 **(D, D')** Top panels (D): Montage showing Sqh-mCherry in the ventral cross-section view of
1353 wild type and *shi*^{ts} embryos during ventral furrow formation. Bottom panels (D'): En face
1354 view images showing myosin accumulation at the indicated time points. En face view images
1355 were Gaussian filtered with a radius of 0.5 pixel. Contrasts were adjusted to make the
1356 cytoplasmic background comparable. Scale bars, 10 μm. Embryos were placed at restrictive
1357 temperature (32ºC) during cellularization. *shi*^{ts} mutant embryos (N = 17 embryos) exhibit
1358 ventral furrow formation defects with different level of severity compared to wildtype
1359 controls (N = 5 embryos). *shi*^{ts} (mild) embryos (N = 10 embryos) progress slower in ventral
1360 furrow formation while *shi*^{ts} (severe) embryos (N = 7 embryos) fail to form ventral furrow as
1361 tissue relaxes after initial constriction. In both group of mutant embryos, apical myosin
1362 intensity eventually rises to a level comparable or higher than that in the wildtype controls.
1363 Interestingly, a previous study has shown that blocking endocytosis using *shi*^{ts} in *snail* mutant

1364 embryos rescued the accumulation of Fog in the apical cytoplasm and partially restored
1365 apical Myosin II accumulation (Pouille et al., 2009). It is unclear whether the Myosin II
1366 phenotype observed in our study was associated with the role of dynamin in regulating Fog.
1367 **(E, E')** Disruption of dynamin function does not prevent apical accumulation of Rab11
1368 vesicles. (E) En face view (maximum projection over 2 μm from apical surface) of the ventral
1369 region of embryos at the onset of gastrulation (T = 0) or during gastrulation when ventral
1370 furrow shows similar morphology between different groups of embryos. (E') Zoom-in view
1371 of the highlighted regions (red boxes) are shown at the bottom. *shi*^{ts} (mild) embryos show
1372 similar apical Rab11 vesicle accumulation compared to the controls. In *shi*^{ts} (severe)
1373 embryos, Rab11 vesicles are already present in the broad apical region of the embryo before
1374 apical constriction starts. Nevertheless, the amount of apical Rab11 vesicles substantially
1375 increases in the constricting cells during ventral furrow formation. Contrasts were adjusted to
1376 make the cytoplasmic background comparable. Images were Gaussian filtered with a radius
1377 of 0.7 pixel. Scale bar, 10 μm. Scale bar for zoom-in panel, 2 μm.
1378

1379 **Supplemental Figure 3**

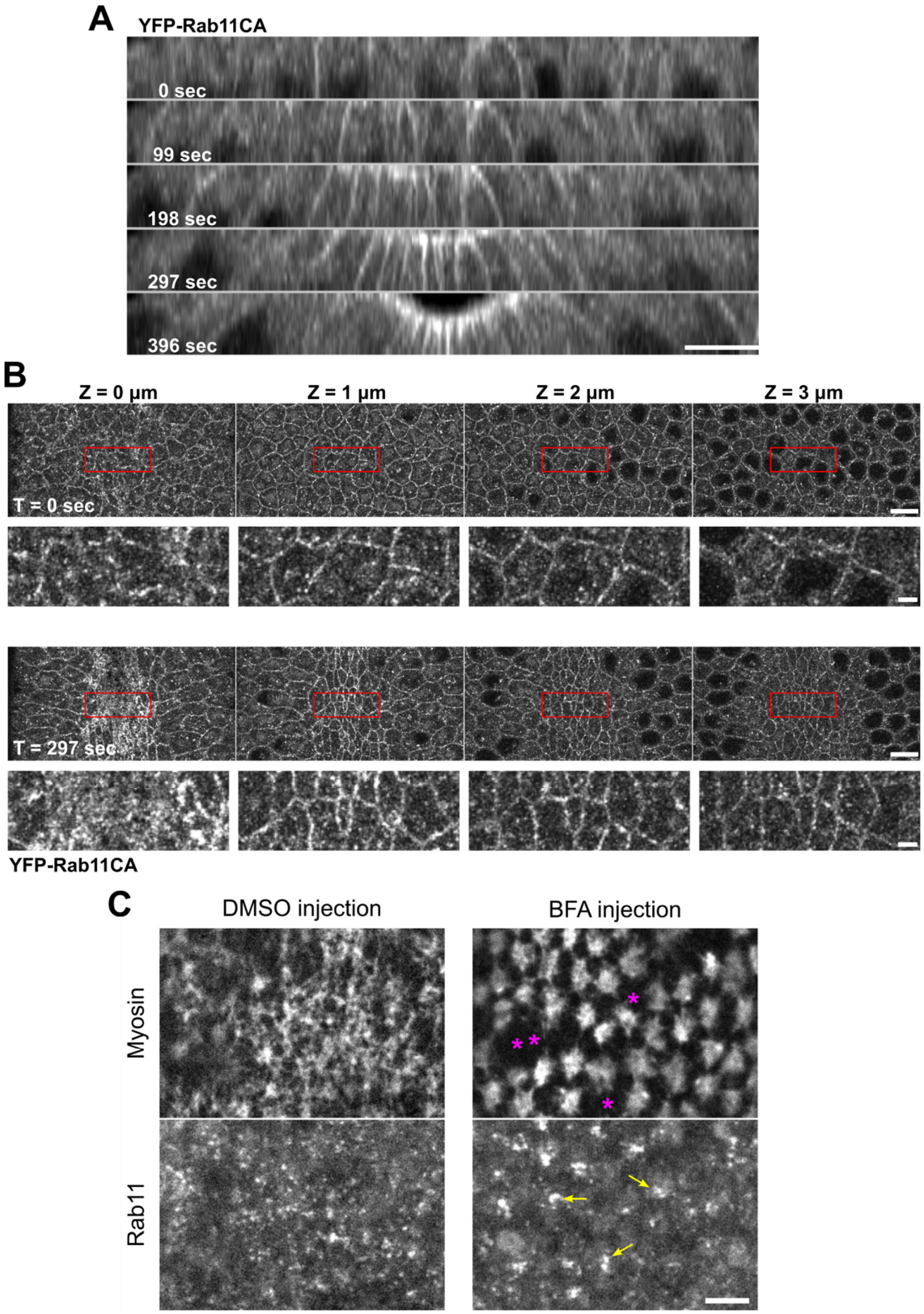

1380

1381 **Figure S3. Rab11 vesicles are likely involved in the exocytic pathways**

1382 **(A, B)** Constitutively active Rab11 localizes to the plasma membrane in addition to vesicles

1383 and perinuclear compartments. (A) Montage showing the cross-section view of an embryo

1384 expressing YFP-Rab11CA during early ventral furrow formation. T = 0 sec indicates the

1385 onset of apical constriction. Apical and lateral membrane localization of Rab11CA is

1386 enhanced over time in the constricting cells. N = 4 embryos. Scale bar, 10 μm. (B) En face

1387 view of the same embryo at T = 0 sec and 297 sec from the apical surface (0 μm) to 4 μm

1388 below the surface. Scale bar, 10 μm. Bottom panels for each time point shows enlarged view

1389 of regions indicated by red boxes. Scale bar, 2 μm.

1390 **(C)** Acute inhibition of secretory pathway by Brefeldin A injection results in enlarged Rab11

1391 structures (yellow arrows) compared to control DMSO injection. Breaks between

1392 neighboring myosin (magenta asterisks) was often observed in BFA injected embryos. N = 3

1393 embryos. Scale bar, 5 μm.

1394 **Supplemental Figure 4**

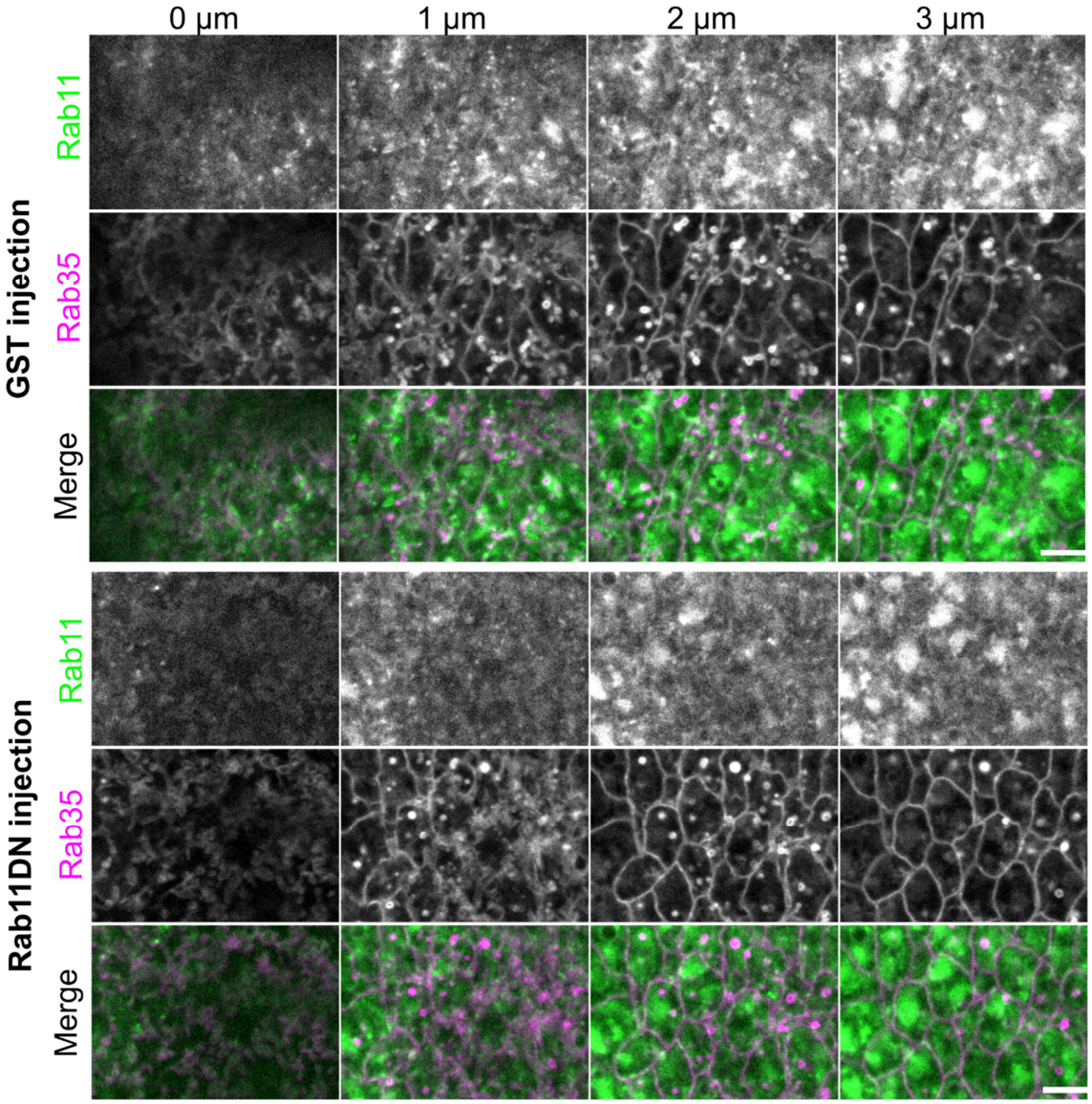

1395
1396

1397 **Figure S4. Rab11DN injection does not affect the Rab35 compartments during apical**

1398 **constriction.**

1399 Eliminating apical Rab11 vesicle accumulation by Rab11DN injection does not prevent the

1400 formation of Rab35 positive tubules or obviously affect their morphology in the constricting

1401 cells during ventral furrow formation. Scale bar, 5 µm.

Supplemental Figure 5

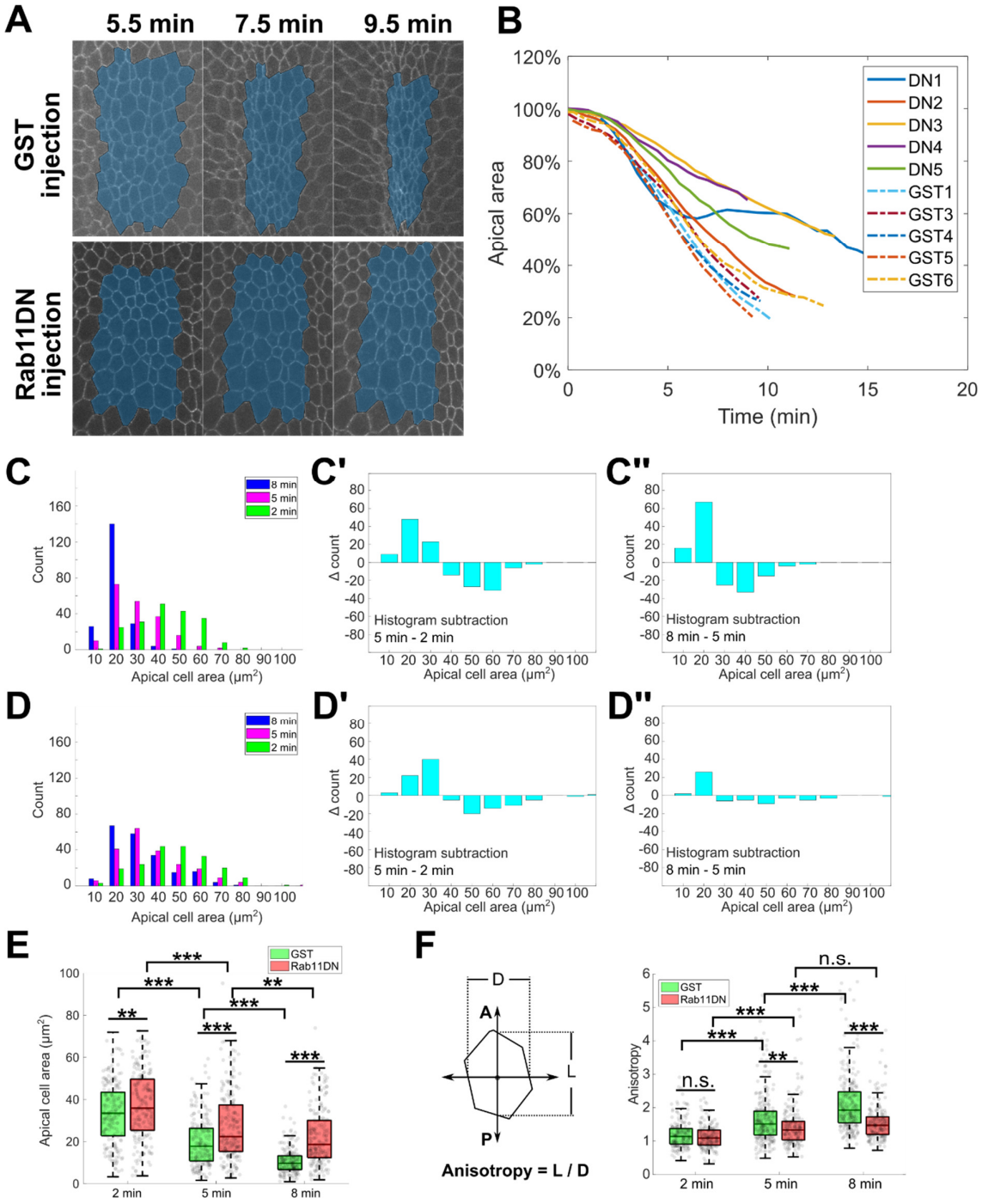

1404 **Figure S5. Acute inhibition of Rab11 results in reduced rate of apical constriction**

1405 **(A)** Representative images showing apical cell area change in GST injected embryo and
1406 Rab11DN injected embryo during apical constriction. A single z plane at 3-4 μm depth from
1407 the apical surface is shown. The total area of a cell group (masked in blue) located in the
1408 middle of the constriction domain was tracked over time and quantified in (B).

1409 **(B)** Apical area change over time. 5 embryos were injected with Rab11DN (DN1-DN5) and 6
1410 embryos were injected with GST (GST1-GST6). The GST2 embryo was not used for
1411 quantification because it exhibited abnormal cell shape even before gastrulation.

1412 **(C-D)** Histograms of individual cell area distribution at 2min, 5min and 8min after the onset
1413 of gastrulation for GST (C, N = 4 embryos, GST1 embryo was not included due to lack of
1414 data at 2 min) and Rab11DN (D, N = 5 embryos) injected embryos. The change in area
1415 distribution is reflected by histogram subtraction between neighboring time points in the
1416 corresponding background (C', C'', D', D''). In the 2 – 5 minute period, apical area reduction
1417 in GST (C') and Rab11DN (D') injected embryos is in general comparable. However, in the 5
1418 – 8 minute period, while cells in GST (C'') injected embryos continue to reduce their apical
1419 area, cells in Rab11DN (D'') injected embryos only show a very mild area reduction.

1420 **(E)** Box plot showing the average cell area at indicated time point for GST and Rab11DN
1421 injected embryos. Two tailed Student's t-test was used for statistical comparison.

1422 **(F)** Quantification of anisotropy for individual constricting cells at 2 min, 5 min and 8 min
1423 after the onset of gastrulation. Same embryos from C-E were analyzed. Compared to GST
1424 injected control embryos, Rab11DN injected embryos show a substantially attenuated

1425 increase in anisotropy in the 5 – 8 minute period. Error bars stand for standard deviation.

1426 Two tailed Student's t-test was used for statistical comparison.

1427

1428 **Supplemental Videos:**

1429

1430 **Video 1. Acute cytoD injection results in rapid tissue relaxation without immediately**

1431 **eliminating apical Myosin II.** 5 mg/mL cytoD was injected into embryo after onset of

1432 apical constriction. A maximum intensity projection of 3 µm of Myosin II signal is shown.

1433 Images were acquired every 9 s and the video is displayed at 10 frames per second.

1434

1435 **Video 2. Endocytosed FM4-64 vesicle colocalizes with Rab5 vesicle but not Rab11**

1436 **vesicles.** 0.5 µg/µL FM4-64 was injected into the embryo at late cellularization. Images were

1437 acquired every 0.46 s during apical constriction and videos are displayed at 20 frames per

1438 second.

1439

1440 **Video 3. Acute disruption of MTs inhibits Rab11 vesicle transport.** A representative

1441 embryo immediately before (top) or one minute after (bottom) 25 mM colchicine injection is

1442 shown. Images were acquired every 0.22 s during apical constriction and videos are displayed

1443 at 20 frames per second.

1444

1445 **Video 4. Acute inactivation of Dynein inhibits Rab11 vesicle transport.** Top, Rab11

1446 channel at indicated time after antibody injection; bottom, same corresponding movies

1447 overlaid with manually segmented trajectories, with red being apically directed transport and

1448 green being basally directed transport. 2 mg/mL antibody was injected during apical

1449 constriction. Scale bar, 2 μm. Images were acquired every 0.22 s during apical constriction
1450 and videos are displayed at 20 frames per second.
1451
1452 **Video 5. Rab11 vesicle dynamics near apical adherens junctions (marked by E-**
1453 **cadherin-GFP).** Rab11 vesicles are moving towards and become enriched at adherens
1454 junctions. Scale bar, 4 μm. Images were acquired every 0.21 s during apical constriction and
1455 videos are displayed at 20 frames per second.
1456
1457 **Video 6. Rab11 vesicles disappear after Rab11DN injection.** Maximum intensity
1458 projections of 3 μm Z stacks from apical surface. GST injection does not affect apical Rab11
1459 vesicle accumulation. Upon Rab11DN injection, however, the apically accumulated Rab11
1460 vesicles disappear over a 4-minute period, while the perinuclear Rab11 compartments appear
1461 to be intact. An exponential fit pixel-wise bleach correction method (ImageJ) was used to
1462 correct for photobleaching. Images were acquired every 5.8 s (left) or 7.2 s during apical
1463 constriction and videos are displayed at 10 frames per second.
1464
1465 **Video 7. Injection of Rab11DN causes frequent breaks in supracellular actomyosin**
1466 **network.** First part of the movie: Increased breaks in apical myosin network. Stars mark the
1467 site where myosin break events happen. Images were acquired every 5.8 s (left) or 5 s (right)
1468 during apical constriction and videos are displayed at 5 frames per second. Second part of the
1469 movie: Increased breaks in apical F-actin networks. Images were acquired every 6 s (top) or 7

1470 s (bottom) during apical constriction and videos are displayed at 5 frames per second.

1471

1472 **Video 8. Acute dynein inhibition by dynein antibody injection affects apical Rab11**

1473 **vesicle accumulation and causes frequent Myosin II breaks.** Dynein antibody was injected

1474 around onset of apical constriction or slightly after. Images were acquired every 4.1 s (top) or

1475 4.7 s (bottom) during apical constriction and videos are displayed at 5 frames per second.

1476

1477 **Video 9. Brefeldin A injection results in abnormal Rab11 structures and frequent**

1478 **Myosin II breaks.** BFA was injected around late cellularization. Images were acquired every

1479 30 s during apical constriction and videos are displayed at 2 frames per second.

1480

1481 **Video 10. Knockdown of Canoe causes frequent Myosin II breaks.** Images were acquired

1482 every 5 s and the video is displayed at 10 frames per second.

1483